



# Chronology and geochemical composition of cassiterite and zircon from the Maodeng Sn-Cu deposit, Northeastern China: Implications for magmatic-hydrothermal evolution and ore-forming process

Xinkai Chen <sup>a</sup>, Zhenhua Zhou <sup>a,\*</sup>, Jiaqi Zhao <sup>a</sup>, Xu Gao <sup>a,b</sup>

<sup>a</sup> MNR Key Laboratory of Metallogeny and Mineral Assessment, Institute of Mineral Resources, CAGS, Beijing 100037, China

<sup>b</sup> Institut für Mineralogie, Leibniz Universität Hannover, Callinstr. 3, 30167 Hannover, Germany



## ARTICLE INFO

### Keywords:

LA-ICP-MS U-Pb dating  
*In situ* micro-area geochemistry  
 Magmatic oxidation state  
 Sn-Cu deposits  
 NE China

## ABSTRACT

Primary tin deposits usually contain little or no copper due to the distinct geochemistry of Sn and Cu. However, examples of copper-rich tin deposits in many tin provinces around the world are also well known. The genesis of copper-rich tin deposits remains controversial. The Maodeng Sn-Cu polymetallic, a typical Cu-rich Sn deposit in the southern Great Xing'an Range (SGXR) Northeast China, offers an excellent opportunity to reveal the genesis of coupled copper-tin deposits. The ore mineralization is associated with the granite porphyry, complement phase of the Alubaogeshan complex, which emplaced into the volcanic rocks of the Lower Permian Dashizhai Formation. Herein, we report new zircon and cassiterite U-Pb ages and their trace elements compositions, with the aim of constraining the metallogenetic chronology framework, and clarifying the indicative effects of the ore-forming fluids on mineralization in different ore-forming stages, and thus establishing the genetic model for the Sn-Cu deposit. LA-ICP-MS U-Pb dating of zircon from the granite porphyry yields a weighted mean U-Pb age of  $134.6 \pm 0.4$  Ma, which consistent to the zircon U-Pb age (ca. 138 Ma) of porphyry monzogranite (main phase of the Alubaogeshan complex) and cassiterite U-Pb ages (137–140 Ma), suggesting an Early Cretaceous Sn-Cu mineralization under the Paleo-Pacific plate slab roll-back setting. Granite porphyry displays more evolved characteristics, with higher SiO<sub>2</sub> contents (71.5 ~ 77.4 wt%), Rb/Sr ratios (3.39 ~ 10.33) and lower Nb/Ta ratios (10.86 ~ 13.06) compared to those of porphyry monzogranite (SiO<sub>2</sub> contents of 70.4 ~ 72.1 wt%; Rb/Sr and Nb/Ta ratios of 1.03 ~ 1.72 and 13.34 ~ 15.83, respectively). This is further supported by the trace elements contents of zircons from granite porphyry and porphyry monzogranite, because the former has a stronger Eu anomaly, higher Hf concentrations, lower Zr/Hf and Th/U ratios than the latter. Our new data, integrated with previously published geochemical data, suggest that the granites associated with Cu-rich Sn deposits are characterized by higher oxygen fugacity, lower differential degree and aluminum saturation index (ASI) than those of Sn-W deposits. This could also use to address the Sn-Cu deposits usually have relatively small Sn mineralization potential. The trace elements of the cassiterites are characterized by high Fe (up to 3358 ppm), Ti (up to 1894 ppm) and abnormal high In (~2500 ppm) concentrations, but low Nb, Ta contents. From early to late stage, the W and U contents and Nb/Ta and Zr/Hf ratios are increased, reveal that the ore-forming process experienced the cooling, increasing volatile contents and fluid-rock reaction. Finally, a new metallogenetic model was established, which highlight oxidized Cu-rich fluids exsolved from the upwelling mantle magma would add to the reduced, Sn-rich magma chambers. This contribution indicate that, the Cu and Sn metals come from the mantle magma and crustal granitic magma, respectively, and that Cu-rich Sn deposits are more likely a product of spatial coupling.

## 1. Introduction

Tin is an indispensable metal in the cutting-edge technology fields

such as new materials, clean energy, information technology, aerodynamics and astronautics (Mao et al., 2019a; Jiang et al., 2019). Tin deposits are mainly associated with polymetallic mineralization (e.g.,

\* Corresponding author.

E-mail address: [zhzhoucags@sina.com](mailto:zhzhoucags@sina.com) (Z. Zhou).

Sn-W-Nb-Ta-Bi-Mo-Pb-Zn-Ag), which generally show clear horizontal and vertical mineralization zoning (Taylor, 1979; Lehmann, 1990; Černý et al., 2005; Mao et al., 2013, 2019b). Previous studies have shown that Sn deposits generated by reduced, ilmenite-series magmas of mainly metasedimentary crustal parentage (Ishihara, 1981; Lehmann, 1990; Blevin et al., 1996), and inversely, Cu deposits formed by oxidized, magnetite-series magmas derived from the mantle (Richards, 2011; Sun et al., 2015). Consequently, the metallogenetic separation of Sn and Cu deposits seems to be a common situation and Sn deposits should typically have relatively minor, subeconomic Cu contents (Sillitoe and Lehmann, 2022). However, co-existing Sn and Cu mineralization are often observed in a single deposit and a subset of deposits contains considerable Cu resources (e.g., pre-eminent Gejiu Sn-Cu district, southern China, Zhao et al., 2021; world-class San Rafael Sn-Cu deposit, southeast Peru, Harlaux et al., 2020), which is seemingly contrary to oxygen fugacity controls on Sn-Cu metallogenesis. To date, it's still uncertain where the Cu originates, and how is it incorporated into the ore-forming fluids, as well as whether the association of oxygen fugacity and ore type is coincidental or not.

In the past decades, numerous large to super-large Sn deposits (e.g., Weilasitu, Baiyinchagan, Huanggang, Xiaogushan, Dajing) have been discovered in the southern Great Xing'an Range (SGXR), northeastern China (Fig. 1), which has been proposed to be a new important tin province in China (Mao et al., 2019b; Zhou and Mao, 2022). The ore-forming ages are mainly in the range of 149 to 133 Ma, and the related granitoids are in an age range of 150 to 135 Ma (Mao et al., 2019b and references therein). The tin deposits are associated with A- or I-type granitoids and cogenetic volcanic rocks, comparable with the tin

deposits in the Central Andean tin belt (Sillitoe et al., 1975; Sillitoe and Lehmann, 2022). The cassiterite- and sulfide-bearing veins are the most important ore type in the SGXR, although there are some skarn, greisen, and porphyry Sn ores. Among these Sn ores are several Cu-rich Sn deposits, e.g., Dajing, Maodeng, Yuanlinzi (Fig. 1), which provide an ideal place for further study of Sn-Cu coupling mineralization process.

The Maodeng Sn-Cu deposit is situated at the western slope of SGXR (Fig. 1b), with ore reserves of 1.14 Mt average grading 1.26 % Sn and 1.85 % Cu (Zhou et al., 2022a), which is a typical high grade, lode-type Cu-rich Sn deposit in the SGXR. Previously published literatures mainly focused on the geological characteristics (Liu, 1996a, 1996b), timing of magmatic-hydrothermal events (Cheng et al., 2014; Ji et al., 2021a, 2021b; Guo et al., 2019), and petrogenesis of intrusions (Wang et al., 1996; Ji et al., 2021a). However, elaborate studies on magmatic property, hydrothermal fluid evolution and ore-forming process are lacking. In this contribution, systematic analyses of in situ zircon and cassiterite LA-ICP-MS U-Pb dating and trace elements analysis were carried out for the Maodeng Sn-Cu deposit. Combined with published studies, we use these data to 1) constrain the formation timing of the magmatism and mineralization, as well as the correlating tectonic setting; 2) decipher the magmatic evolution process involving crystal fractionation, and the adding of oxidized fluids exsolved from mafic magmas to Sn-bearing fluids; and 3) throw new insights into the coupling Sn-Cu precipitation mechanism from trace element variations in cassiterite.

## 2. Geological background

The SGXR is located in the eastern part of Inner Mongolia,

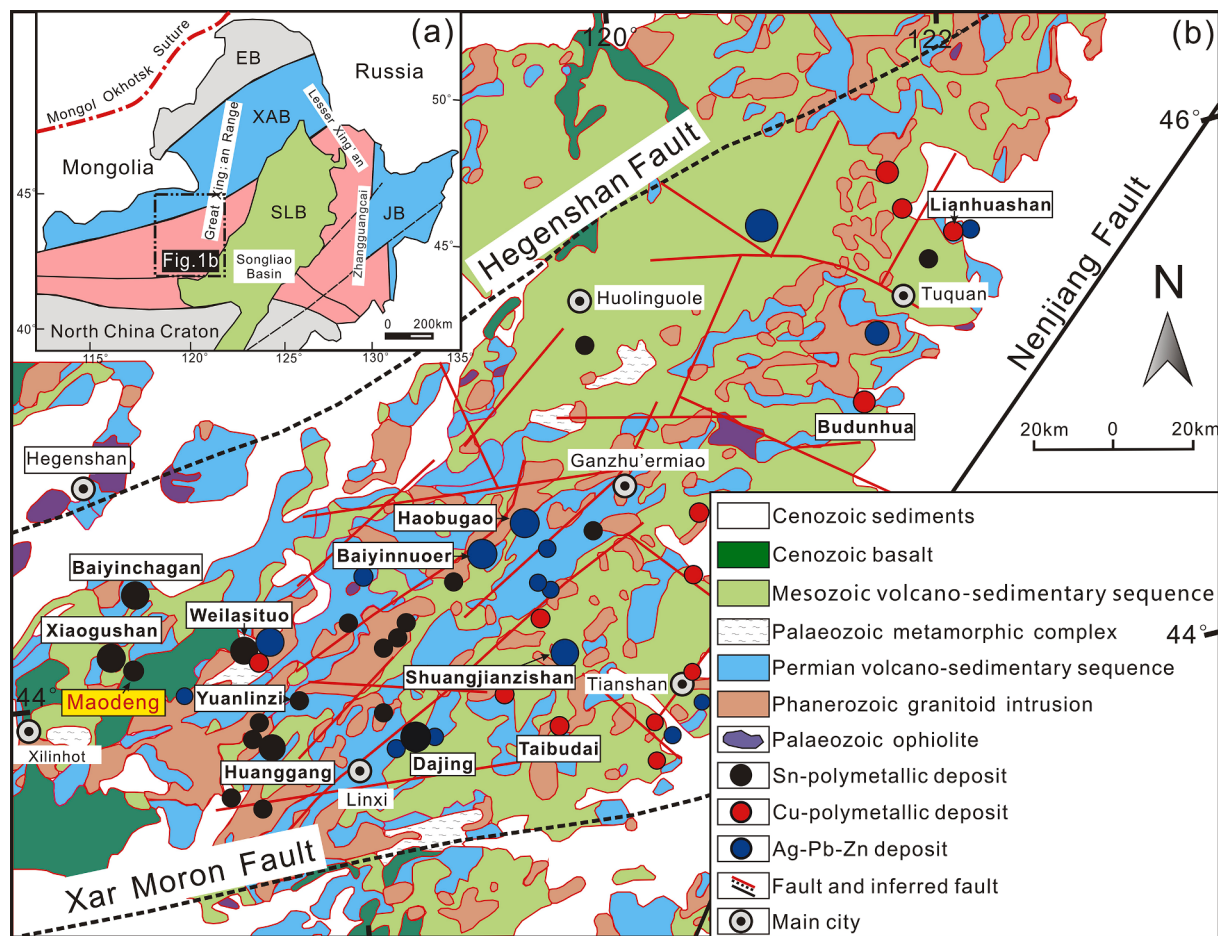


**Fig. 1.** (a) Simplified geotectonic division of the northeastern China; (b) Geological and ore deposit distribution map of southern Great Xing'an Range (modified after Ouyang et al., 2015).

northeastern China, bordered by the Hegenshan fault in the north, the Xar Moron fault in the south, and the Nenjiang fault in the southeast (Fig. 1b). The SGXR is considered to include many remnants of microcontinents, ophiolite belts, tectonically related magmatic arcs, and fore- or back-arc basins (Şengör et al., 1993; Xiao et al., 2009). It records the late Paleozoic to Early–Mid Triassic closure of the Paleo-Asian Ocean and the subsequent Mesozoic subduction of the West Pacific Plate beneath the Eurasian continent (Xiao et al., 2009). The principal sets of NE- to NNE- and NW-striking faults, together with E-W-striking basement faults, constitute a triangular structural framework (Zhou et al., 2022b).

The Precambrian basement rocks in the SGXR constitute a khondalitic sequence of sillimanite- and garnet-bearing gneisses, hornblende-plagioclase gneisses and felsic ortho- and paragneisses (Zhou et al., 2011). The Early Paleozoic medium- to high-grade metamorphic complex of the Xilingol Comolex constitutes the oldest formation in this area (Shi et al., 2003), with the  $^{206}\text{Pb}/^{238}\text{U}$  ages of zircons from 494 to 402 Ma (Li et al., 2017a, 2017b). The Ordovician to Carboniferous strata are composed mainly of detrital metasedimentary units, carbonate rocks, and volcanic rocks (Wang et al., 2001). Permian mafic to intermediate-felsic volcanic rocks are well developed and constitute the ore-hosting rocks for most Sn deposits in the region (Wang et al., 2001). Mesozoic volcanic-sedimentary sequences comprise this area's major cover, consisting of intermediate-felsic volcanic rocks.

Phanerozoic granitoids are widely distributed in the area, including two episodes of magmatism: 1) late Paleozoic (321–260 Ma), with rock assemblages are diorite-tonalite-granodiorite (Wu et al., 2011; Ouyang et al., 2015). These rocks are mainly developed in western SGXR and only few of them are related to ore mineralization (Zhou and Wilde, 2013); and 2) Late Mesozoic (150–130 Ma), mainly composed of granodiorite, biotite granite, monzogranite, granite porphyry, K-feldspar granite and syenite porphyry (Wu et al., 2011). They mainly occur as batholith or stock, and are closely related to polymetallic mineralization in the area (Zhou and Mao, 2022). The SGXR includes a variety of polymetallic deposits characterized by the symbiosis of polymetallic elements. Previous studies have classified the mineralization in the SGXR from east to west as Cu-polymetallic, Ag-Pb-Zn polymetallic and Sn-polymetallic series, based on the location of the deposits' output (Ouyang et al., 2013, 2015), which show the typically regional metallogenetic zoning. Copper-polymetallic deposits are mainly distributed in eastern slope of the SGXR (Fig. 1b), include Taibudai (40,852 t at 1.5 % Cu; Zhou et al., 2015), Budunhua (0.2 Mt at 0.6–1.88 % Cu; Ouyang et al., 2014), Lianhuashan (0.13 Mt at 0.93 % Cu; Ouyang et al., 2015), etc. Silver-lead-zinc polymetallic deposits are situated along a NE-trending normal fault system, mainly distributed in Linxi-Ganzhu'er-miao area, and representative deposits include Baiyinnuoer (1.78 Mt at 5.73–8.67 % Zn, 0.66 Mt at 1.72–2.09 % Pb, 1027 t Ag; Shu et al., 2013), Shuangjianzishan (21700 t Ag at 128 g/t, 1.1 Mt at 1.2 % Zn, 3.3 Mt at 1.2 % Pb; Zhai et al., 2020), Haobugao (0.29 Mt at 4.24 % Zn, 0.15 Mt at 2.25 % Pb; Shu et al., 2021). The Sn-polymetallic deposits are mainly distributed in the western slopes of the SGXR, including several large Sn deposits (e.g., Weilasituo: 83,700 t at 0.89 % Sn, Baiyinchagan: 0.22 Mt at 0.76 % Sn, Huanggang: 0.46 Mt at 0.29 % Sn) and tens of middle and small scales tin deposits (Mao et al., 2019b). Spatially, these deposits show a NE-trend distribution that exhibit the structural ore-controlling characteristics.

### 3. Geology of the Maodeng Sn-Cu deposit

The Maodeng deposit (longitude  $116^{\circ}33'44''$ – $116^{\circ}35'03''$  E, latitude  $44^{\circ}10'05''$ – $44^{\circ}10'59''$  N) is located 50 km northeast to the Xilinhot city, Inner Mongolia, NE China. Country rocks in the deposit include Lower Permian Dashizhai and Shoushangou Formations, comprising sandstones and medium-acidic volcanic rocks; Lower Jurassic Hongqi Formation, Middle Jurassic Manitu Formation and Lower Cretaceous Baiyingaolao Formation, mainly including clastic rocks, medium acidic

volcanic rocks, and siltstones, respectively, and Quaternary alluvial deposits (Fig. 2a). The structural framework of this ore field includes well-developed faults in NE-trending, NW-trending, and E-W-trending sets, with numerous secondary faults and fractures. Three strike-parallel compressive fractures (FI-2, FII-35, FII-46) being the main faults, with a strike of  $315^{\circ}$ – $335^{\circ}$ , NE-trending and a dipping angle of  $60^{\circ}$ – $85^{\circ}$ . A large number of fissure zones are developed between these main faults, which are divided into I, II and III fault zones from west to east (Fig. 2b). These faults are the main ore-hosting structures and control the occurrence of major orebodies.

Magmatic rocks exposed in the ore district are the Alubaogeshan complex, with gabbro occurring occasionally in the southwest. The Early Cretaceous Alubaogeshan complex, located in the west part of the ore district, is mainly composed of porphyry monzogranite and granite porphyry. The granitic complex intrudes into Dashizhai Formation, Hongqi Formation and Baiyingaolao Formation in an irregular round shape (Fig. 2a), with the outcrop area of porphyry monzogranite (ca.  $42 \text{ km}^2$ ) is much larger than those of granite porphyry (ca.  $7 \text{ km}^2$ ), the Sn-Cu mineralization whereas is concentrated in the latter. Porphyry monzogranite is the main intrusive phase rocks of the Alubaogeshan complex, while the granite porphyry intrudes on the west side of the porphyry monzogranite with the characteristics of shallow-ultrashallow intrusion, which is identified as complement phase here. Furthermore, there is no clear contact relationship between the intrusive rocks of two lithologies.

Hydrothermal alteration is widespread at Maodeng, with the most intense alteration occurring in and around mineralized Sn-Cu veins. Silicification, greisenization and potassie alteration are the most common alteration in the ore district, sericitization and chloritization alteration occur only in the granite porphyry in the fault zone III (Fig. 2b). Alteration halos are distributed intensively on either side of the mineralized veins. Components of these alteration assemblages are mainly quartz, K-feldspar, biotite, sericite and chlorite. Silicification is the most widespread expression of alteration type in the ore field (Fig. 3a), mainly occurs in the form of quartz veins and contains various sulfides in the ore district (e.g., molybdenite, chalcopyrite, pyrite and arsenopyrite). Greisenization occurs in the wall rock of granite porphyry as vein, usually associated with Sn mineralization (Fig. 3b). Potassie alteration is widely developed in granite porphyry (fault zone III), the main altered minerals are K-feldspar and biotite, while in wall rock develops in vein alteration near the Sn-Cu mineralized veins (fault zone I, II), the altered mineral assemblages are mainly biotite and quartz, and K-feldspar is not developed. Moreover, in granite porphyry of the inner contact zone, sericite and quartz metasomatism plagioclase and chlorite metasomatism biotite are found locally, resulting in slight sericitization and chlorite alteration. The outer alteration zone is dominated by silicification, tourmalinization and chloritization, accompanied by a large number of veins, with the ore bodies being mostly of the cassiterite-sulfide-quartz type (Liu 1996a, 1996b). The Sn-Cu ore bodies were banded or vein-like, with a thickness of 50 to 100 m (Fig. 2c).

Ore and gangue minerals can be identified based on field geological surveys and observations. Specifically, ore minerals mainly include cassiterite, chalcopyrite, sphalerite, molybdenite, pyrite, pyrrhotite, wolframite, galena, bornite, chalcocite, and gangue minerals are mainly of quartz, tourmaline, muscovite, fluorite, sericite, chlorite, and calcite. According to the observations of mineral assemblages, textures and interpenetration relationship between veins, mineralization in the Maodeng Sn-Cu deposit can be divided into three stages of vein growth: Quartz-cassiterite (-wolframite) (Stage-I) is represented by the main metallogenetic stage of Sn in the district, with characteristics of cassiterite-chalcopyrite co-existing (Fig. 3c) or cassiterite-chalcopyrite bearing quartz vein cross-cutting wall rock (Fig. 3d). Co-occurrence of the chalcopyrite and cassiterite can be seen in the ores, along with the output of few topaz (Fig. 3e). Base-metal sulfide (Stage-II) is characterized by the presence of large amounts of sulfides such as chalcopyrite, galena, sphalerite, and these metal sulfides are mainly occurred in

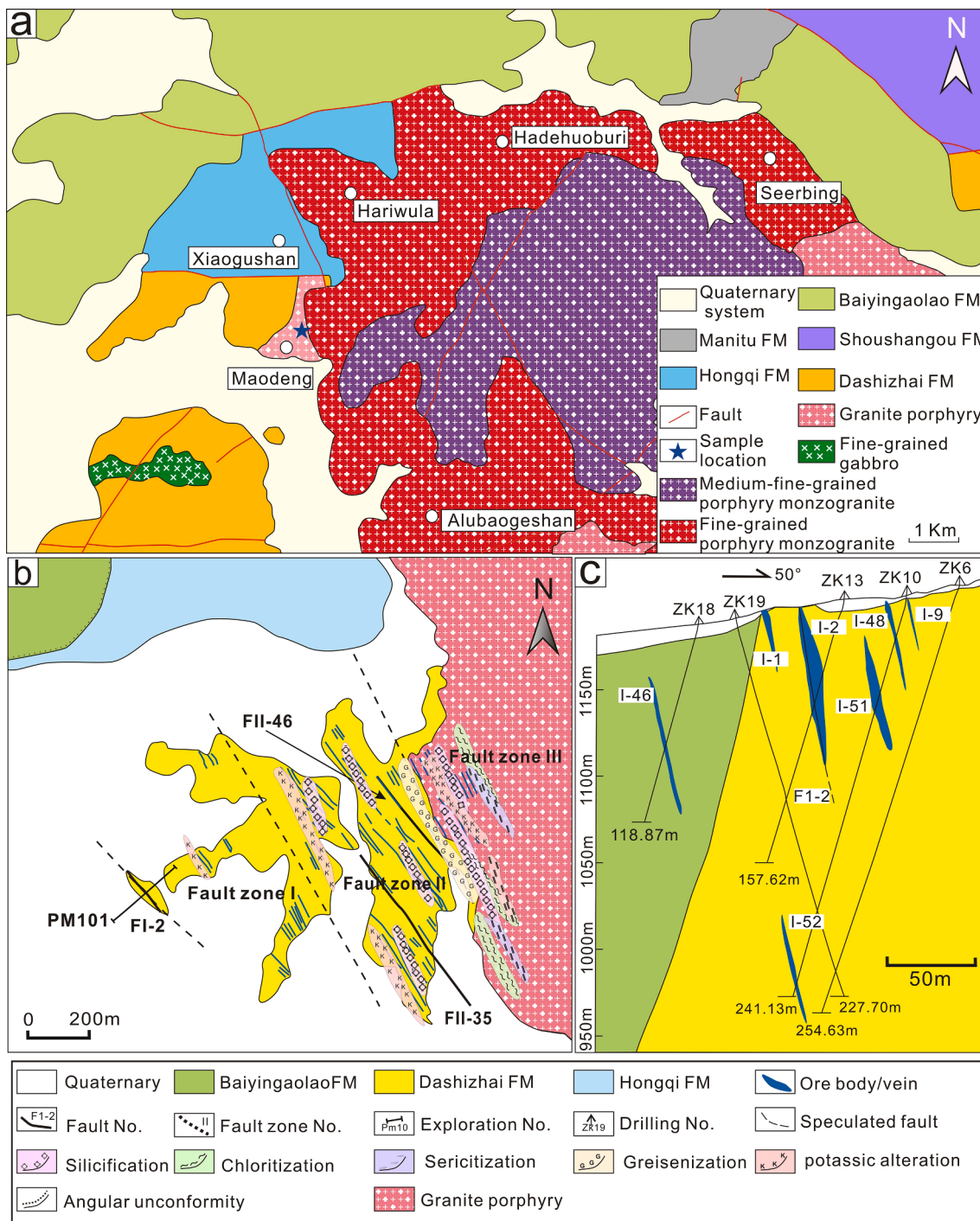


**Fig. 2.** (a) Geological map of the Maodeng-Xiaogushan tin-polymetallic orefield (modified after Zhang et al., 2013); (b) Geological sketch map of the Maodeng Sn-Cu deposit (modified after Guo et al., 2019); (c) Profile of the No. 101 prospecting line of the Maodeng Sn-Cu deposit.

quartz veins (Fig. 3f-g). Late veinlets and crusts (quartz-calcite-fluorite veins) were identified as Stage-III, with characteristics of euhedral coarse cassiterite surrounded by calcite and sphalerite, and complete rim of cassiterites can be observed (Fig. 3g-h) (Ji et al., 2021b; Zhou et al., 2022a). Furthermore, the plagioclase-quartz veins fill into the crevices of cassiterite particles, these cassiterites show the well-integrated rim, indicating they haven't been disturbed by the late hydrothermal fluids. The different interference colors of cassiterites are indicative of its different element contents (Fig. 3i).

#### 4. Petrography

The petrographic characteristics of the mineralized intrusions in the Maodeng ore field were collected based on observations from outcrops. The granitoids, i.e., mainly porphyry monzogranite and granite porphyry, all show typically porphyritic texture and similar minerals. Specifically, granite porphyry is off-white in color, coarse-grained (Fig. 3j), mainly distributed on the edge of the Alubaogeshan complex. It consists of quartz (35–40 vol%), feldspar (25–30 vol%), plagioclase (15–20 vol%) and biotite (3–5 vol%). Plagioclase is subhedral, plate-like structure, and experienced various degrees of sericitization-

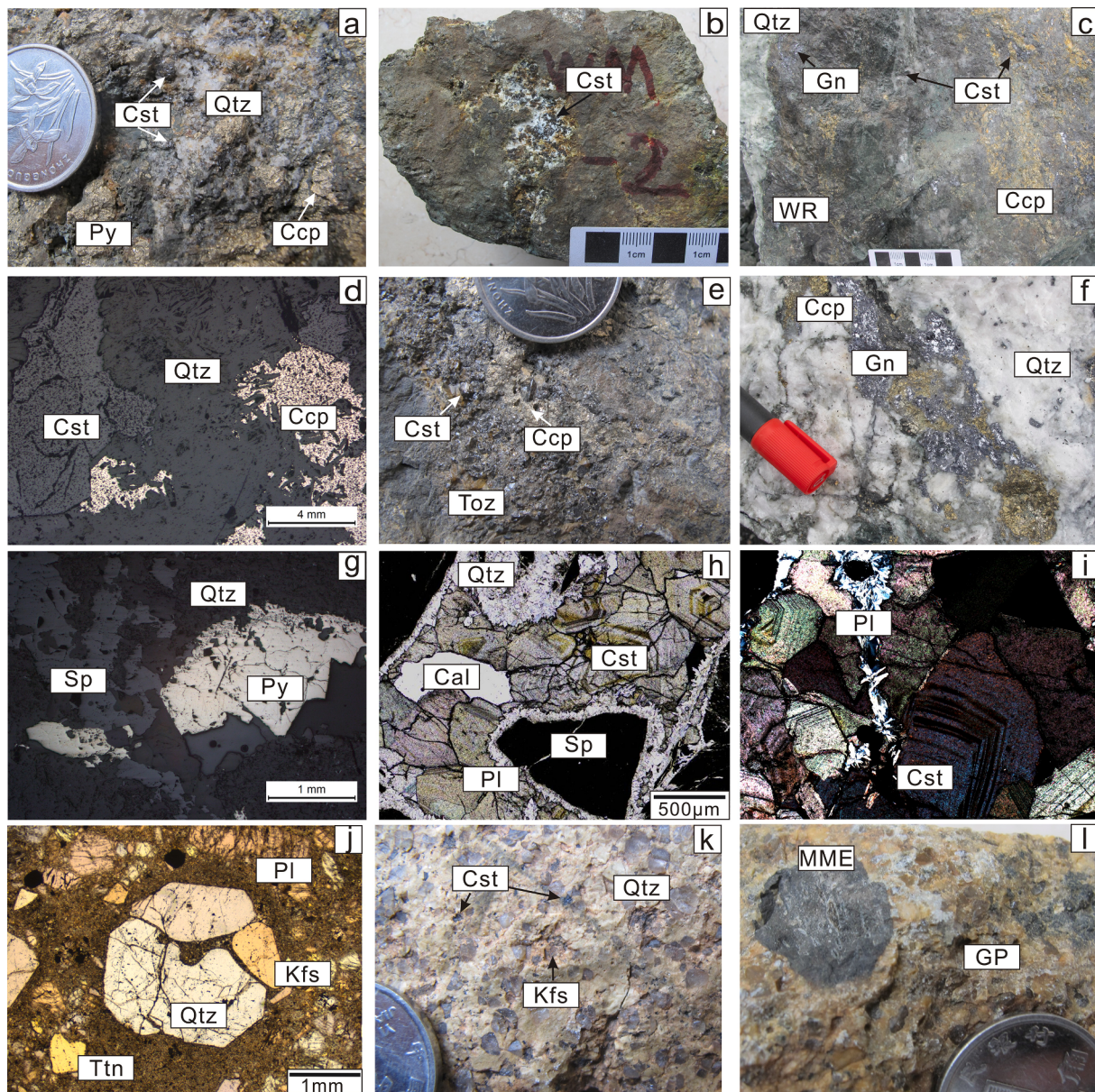


**Fig. 3.** Outcrop and microphotographs of the Maodeng ore field. Silicification (a) and greisenization (b) in the field; (c) cassiterite co-exist with chalcopyrite in wall rock (c) or quartz vein (d-e); (f) chalcopyrite and galena vein in the late sulfide stage, containing; (g) sphalerite-pyrite bearing quartz vein; (h) cassiterite bearing quartz vein with ore sulfide and calcite; (i) complete rim structure of cassiterites; (j) granite porphyry; (k) microphotograph of granite porphyry; (l) MMEs in granite porphyry. Mineral abbreviations: Qtz-quartz; Kfs-K-feldspar; Pl-plagioclase; Ccp-chalcopyrite; Cst-cassiterite; Py-pyrite; Ttn-titanite; Sp-sphalerite; Gn-galena; Toz-topaz; Cal-calcite; MME-mafic microgranular enclave; GP-granite porphyry.

kaolinization. K-feldspar presents automorphic while quartz is xenomorphic, and the surface is more cracks (Fig. 3k); zircon, apatite, sphene, xenotime, ilmenite and magnetite are the common accessories. The matrix is visible as serpentinization, and mafic microgranular enclaves (MMEs) can be seen occasionally (Fig. 3l).

The main phase of the Alubaogeshan complex, porphyry monzogranite, is grey in color, medium-coarse grain texture, with plagioclase (20–30 vol%), K-feldspar (30–40 vol%), quartz (10–15 vol%) and minor hornblende (1–5 vol%). Polysynthetic twin can be seen in plagioclase. Hornblende is locally metasomatized by biotite, and chloritization can be identified in hornblende. Previous studies have also performed mineral EPMA analysis on the Alubaogeshan complex (Liu, 1996a), suggesting the granite porphyry and porphyritic monzogranite may be produced by homologous magmatic evolution. Furthermore, EPMA analyses of biotite and hornblende suggest that the magma has

relatively high H<sub>2</sub>O, F and Cl contents, and evolved under shallow emplacement (Ji et al., 2021a).

## 5. Analytical methods

### 5.1. Zircon U-Pb dating and trace element analyses

Zircon sample pretreatment and analyses were carried out in the MC-ICP-MS laboratory of the Institute of Mineral Resources, Chinese Academy of Geological Sciences (IMR, CAGS). The test samples were crushed to less than 60 mesh under pollution-free conditions, initially sorted by gravity and magnetic methods, and then screened under binocular microscope for zircon with good crystallinity and transparency. The zircon to be tested was placed on double-sided adhesive, fixed with epoxy resin, and finally polished. Before testing, zircon was observed in detail

according to the reflected light, transmitted light and CL images in order to select a suitable test spot. In suit zircon U-Pb isotopic and trace element analysis were undertaken synchronously by LA-ICP-MS. Finnigan Neptune MC-ICP-MS and the accompanying Newwave UP 213 laser exfoliation system were used for the experiment, operated at energy density of about  $2.5 \text{ J/cm}^2$ , frequency of 10 Hz, spot diameter of 25  $\mu\text{m}$ . Laser ablation uses Helium as carrier gas. Zircon U-Pb dating takes GJ-1 ( $607.0 \pm 2.8 \text{ Ma}$ , Jackson et al., 2004) as the external standard, and time-dependent drifts of U-Th-Pb isotopic ratios were corrected using linear interpolation for every batch of bracketed analyses, according to the variations in GJ 1. The concentrations of U, Th, and Pb were calibrated using Zircon M127 with 923 ppm U, 439 ppm Th, and Th/U = 0.475 (Nasdala et al., 2016). Moreover, the zircon sample Plešovice ( $337.1 \pm 0.3 \text{ Ma}$ ; Sláma et al., 2008) is used to calibrate the machine. Ordinary Pb correction is carried out according to the measured  $^{204}\text{Pb}$ . Precision and accuracy for the major and trace elements are 5–10 %. The error of the analysis result is  $1\sigma$ , and the weighted average U-Pb age concordant plot was performed using ISOPLOT 3.70 program (Ludwig, 2003).

### 5.2. Cassiterite U-Pb dating

The test samples were first selected by the gravity separation method, and then the selected samples were selected under binocular microscope. Cassiterite grains that are in good shape are selected for target fabrication. And suitable ones, avoiding inclusions and fissures, are selected for dating based on transmitted light, reflected light and CL images of the cassiterite targets. The cassiterite U-Pb dating was carried out at the Isotope Laboratory of the Tianjin Institute of Geology and Mineralogy, using laser ablation multi-receiver inductively coupled plasma mass spectrometer (LA-MC-ICP-MS), and the accompanying multi-receiver inductively coupled plasma mass spectrometer (Neptune) manufactured by Thermo Fisher for the experiment. With a total of nine Faraday cup receivers and 4 ion counter receivers to ensure experimental accuracy. The laser was a UP193-FX ArF excimer laser from ESI, USA, with a wavelength of 193 nm, pulse width of 5 ns, laser stripping beam of 50  $\mu\text{m}$ , laser energy density of  $10 \text{ J/cm}^2$  and frequency of 20 Hz. AY-4 was used as the standard sample (U content of 30 ppm,  $^{206}\text{Pb}/^{238}\text{U}$  weighted age average of  $158.2 \pm 0.4 \text{ Ma}$ , ID-TIMS; Yuan et al., 2011). Zircon specimens were used as primary standards to calibrate the instrument condition prior to the assay, and then a laboratory cassiterite working standard was used as a secondary standard to alternate with the cassiterite sample being assayed. Initial common lead deductions for non-radiogenic causes were performed by Tera-Wasserburg harmonic plots and corrected for elemental fractionation effects. ICPMSDataCal program (Liu et al., 2010) and Isoplot program (Ludwig, 2003) were used for data processing.

### 5.3. In-situ micro-area trace elements analysis

The cassiterite grains are picked out under a binocular microscope and glued to the epoxy resin, and worn down them until most of the cassiterite grains were exposed after the resin had cured. CL images were carried out on cassiterite target samples, selecting primary oscillatory zones and avoiding inclusions and fissures for the experiment. The in-situ trace element analysis was carried out at the IMR, CAGS. The instrument used is a Resolution S155 193 nm laser ablation system and the accompanying Bruker M90 inductively coupled plasma mass spectrometer (LA-ICP-MS), with a beam spot size of 50  $\mu\text{m}$ , laser energy density of  $6 \text{ J/cm}^2$ , laser frequency of 5 Hz. High purity Helium is used as carrier gas for denudation. The external standard sample used in the in situ analysis of cassiterite is NIST SRM 610. While NIST SRM 612, NIST SRM 614 and GSE-1G standard samples were used as the secondary standards to detect the accuracy of LA-ICP-MS analysis. The analytical results for the standards NIST SRM 610, NIST SRM 612 and NIST SRM 614 showed that the analytical accuracy was below 5 % for trace

elements at around 400 ppm, below 10 % for most trace elements at around 40 ppm (around 15 % for Ti, Ta), and below 15 % for most trace elements at around 0.8 ppm. Most of the trace elements at 0.8 ppm or less were analyzed with less than 15 % accuracy (Wang et al., 2014). The NIST SRM 612 and NIST SRM 614 specimens were in good agreement with the recommended values, and most of the GSE-1G specimens were within 15 % of the recommended values, indicating that the matrix effect was not significant when synthetic glass was used as an external specimen during the test. The poor accuracy of some elements may be due to the fractionation of these elements with respect to the international standards (Günther et al., 1999), or to the inhomogeneity of the standard glass (Eggins and Shelley, 2002).

## 6. Results

### 6.1. Review of bulk rock geochemical compositions

With the purpose of understanding the magmatic evolution and Sn-Cu mineralization process, a complementary dataset (e.g., Cheng et al., 2014; Guo et al., 2019; Ji et al., 2021b) comprising reliable bulk rock major and trace element concentrations for the granite porphyry from the Maodeng Sn-Cu deposit has been complied. These rocks show high  $\text{SiO}_2$  (73.2–77.3 wt%) and total alkalis (ALK;  $\text{Na}_2\text{O} + \text{K}_2\text{O} = 8.00\text{--}8.69 \text{ wt\%}$ ), intermediate  $\text{Al}_2\text{O}_3$  (11.67–12.83 wt%), and relatively low  $\text{MgO}$  (0.12–0.46 wt%),  $\text{TiO}_2$  (0.13–0.27 wt%),  $\text{MnO}$  (0.00–0.05 wt %) and  $\text{P}_2\text{O}_5$  (0.02–0.07 wt%). Their A/CNK [molar  $\text{Al}_2\text{O}_3/(\text{CaO} + \text{K}_2\text{O} + \text{Na}_2\text{O})$ ] values range from 0.97 to 1.04, indicating metaluminous characteristics.

The porphyry monzogranite show relatively higher  $\text{Al}_2\text{O}_3$ ,  $\text{TiO}_2$ ,  $\text{P}_2\text{O}_5$  and ALK (13.64–14.28 wt%, 0.41–0.51 wt%, 0.11–0.14 wt%, and 8.69–8.98 wt%, respectively), lower  $\text{SiO}_2$  (70.4–72.1 wt%) contents, but similar contents of  $\text{MnO}$ ,  $\text{MgO}$  and A/CNK (0.03–0.07 wt%, 0.26–0.47 wt%, and 0.98–1.05, respectively) than the granite porphyry. In addition, the porphyry monzogranite samples show the relatively higher Ba, Sr contents and Eu anomaly, indicate they underwent crystal fractionation of K-feldspar and/or plagioclase.

### 6.2. Zircon and cassiterite U-Pb dating

One zircon (WM-16) and two cassiterite samples (WM-7, WM-8) from the Maodeng deposit were selected for LA-ICP-MS U-Pb dating. The CL images of representative zircons and cassiterites are illustrated in Fig. 4, and the U-Pb dating results are listed in Supplementary Table S1 and plotted on Fig. 5.

The zircon grains are light-yellow, transparent to semi-transparent, and form euhedral stubby to elongate prismatic crystals, with 150–200  $\mu\text{m}$  in length, 50–100  $\mu\text{m}$  in width, and the aspect ratios are between 1:2 and 1:3. They have oscillatory zoning and lack visible inherited cores (Fig. 4a). The contents of Th and U are 26–349 ppm and 62–1072 ppm, respectively, with Th/U ratios of 0.31–0.55. A total of 30 zircons were analyzed, four spots (WM-16-18, WM-16-19, WM-16-24, WM-16-29) were excluded from the concordia plot because that they are discordant (concordance less than 95 %), due to Pb loss or the presence of inclusions or cracks. The remaining 26 analytical spots record a  $^{206}\text{Pb}/^{238}\text{U}$  age range from 132.6 to 139.2 Ma, with a weighted mean  $^{206}\text{Pb}/^{238}\text{U}$  age of  $134.6 \pm 0.7 \text{ Ma}$  (MSWD = 0.55) (Fig. 5a-b).

Cassiterite grains in sample WM-7 (base-metal sulfide stage) are irregular in shape and about 400–700  $\mu\text{m}$  in size. The CL images of the cassiterite samples show bright luminescence with clear oscillatory growth zonation (Fig. 4b), with U concentrations and Th/U ratios of these analyzed grains in the range of 0.05–0.76 ppm and 0.01–0.35, respectively (Supplementary Table S1). Thirty-one analyses were performed and they yield a lower intercept age of  $137 \pm 6 \text{ Ma}$  (MSWD = 3.0) (Fig. 5c).

Cassiterite grains in sample WM-8 (quartz-cassiterite (-wolframite) stage) are also irregular in shape and about 300–600  $\mu\text{m}$  in size. The CL

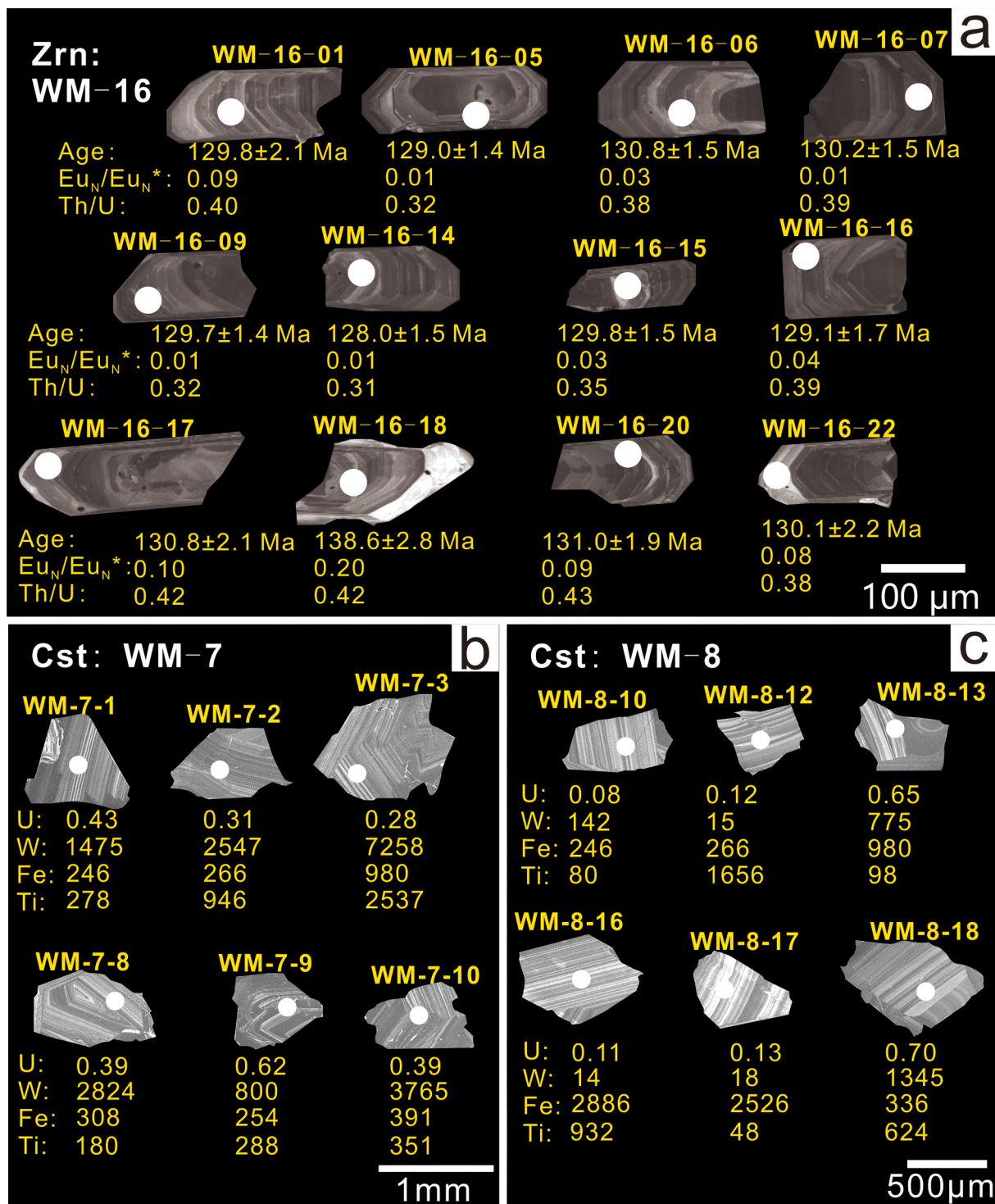


**Fig. 4.** Cathodoluminescence images of representative zircon and cassiterite grains. White solid circles with a radius of 30  $\mu\text{m}$  represents the spots for LA-ICP-MS U-Pb dating and trace elements analysis. (a) zircon sample WM-16, (b) cassiterite sample WM-7, and (c) cassiterite sample WM-8. Abbreviations: Zrn-zircon, Cst-cassiterite.

images show obvious oscillatory growth zonation (Fig. 4c). The U concentrations of these analyzed grains were 0.03–0.77 ppm, with Th/U ratios of 0.002–0.30 (Supplementary Table S1). Forty-six analytical results gave a lower intercept age of  $140 \pm 6 \text{ Ma}$  ( $\text{MSWD} = 3.0$ ) (Fig. 5d).

### 6.3. Trace elements of zircon

The trace elements of zircon samples are listed in Table 1. As in all

microanalytical approaches to mineral chemistry, there is a risk of the analyses reflecting contamination by melt or crystal inclusions. We used elements that are normally found in very low concentrations in zircon to monitor such contamination; i.e., La for LREE-rich minerals and fluid inclusions, Ti for Fe-Ti oxides, and Nb and Ta for coltan (Li et al., 2021a, 2021b). In our study, nine spots (WM-01, WM-16-15, WM-16-19, WM-16-21, WM-16-23, WM-16-24, WM-16-26, WM-16-28, WM-16-29) were excluded due to the possible contamination (high La contents). REE

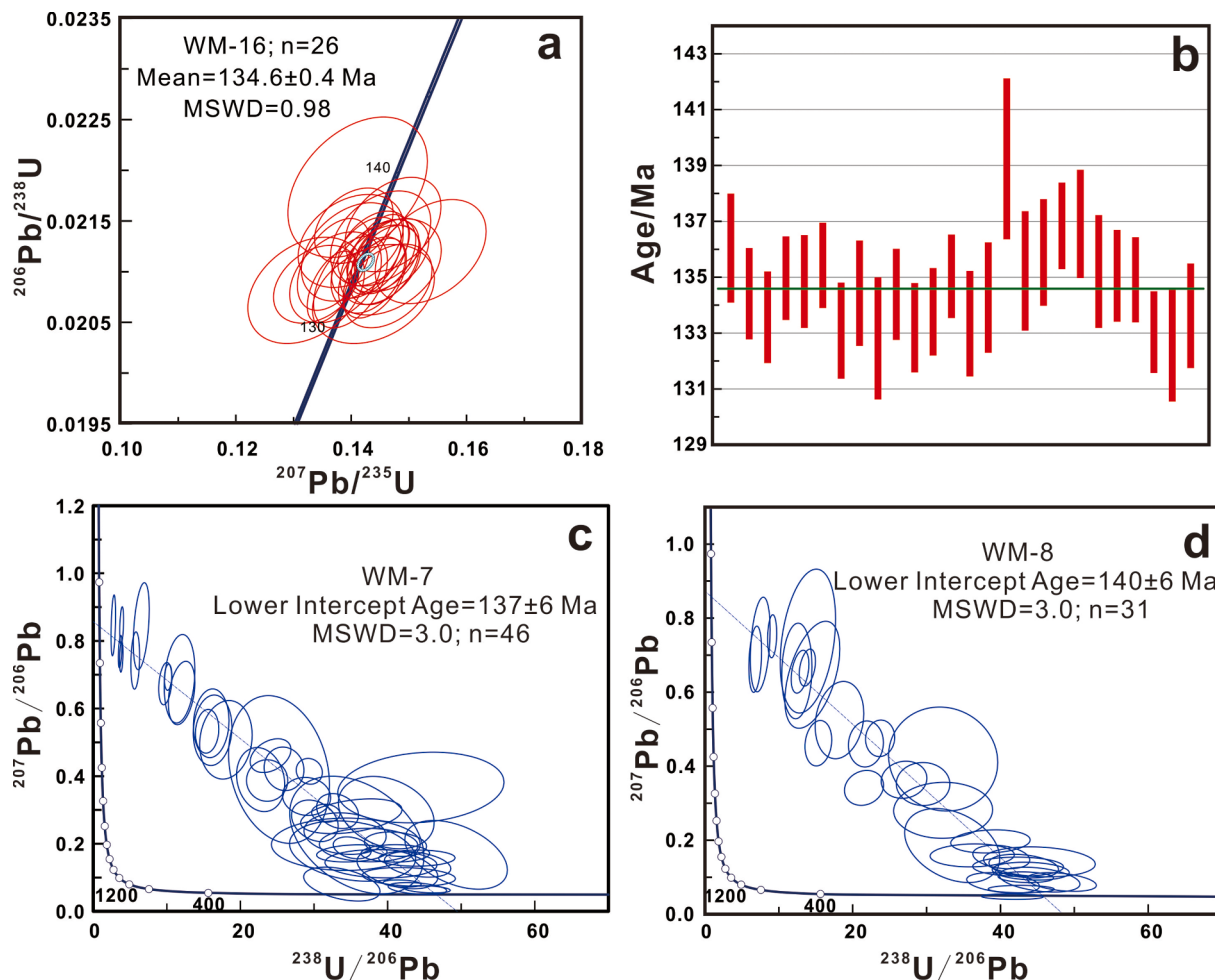


**Fig. 5.** Zircon U-Pb Concordia diagrams (a) and weighted average  $^{206}\text{Pb}/^{238}\text{U}$  ages (b) for the granite porphyry, and Tera-Wasserburg U-Pb plots for cassiterite in Maodeng Sn-Cu deposit. (c) sample WM-8, and (d) sample WM-7.

pattern of ore field shows enrichment of HREE, with moderate contents of REE (270–1094 ppm), positive Ce anomaly ( $\text{Ce}_N/\text{Ce}_{N^*}=5.1\text{--}271.3$ , average = 78.3) and negative Eu anomalies ( $\text{Eu}_N/\text{Eu}_{N^*}=0.01\text{--}0.20$ , average = 0.05) (Fig. 6a–c). The samples also have relatively high and variable Th (26–346 ppm) and U (62–1066 ppm) contents, with Th/U ratios range from 0.31 to 0.54. The characteristics of trace elements variation in zircon are relatively low values of Ce anomaly, Eu anomaly and Zr/Hf (Fig. 6b–d), suggesting the low differentiation.

#### 6.4. Trace elements of cassiterite

Thirty-seven elements have been analyzed for trace element concentrations by LA-ICP-MS. The concentrations of Cr, Rb, REEs and Th are mostly below or near the detection limit. The analytical results for WM-7, WM-8 and MD1901 that above the detection limit are listed in Table 2, representative elements are illustrated in Fig. 10. Cassiterite grains show generally high concentrations of Fe (152–5133 ppm, average = 1535 ppm), In (2004–2702 ppm, average = 2335 ppm), Ti (9–3788 ppm, average = 692 ppm), and W (1.2–7603 ppm, average = 1085 ppm), while are characterized by low concentrations of high field strength elements (HFSEs), with Nb ranging from 0.01 to 11.43 ppm (average = 0.6 ppm), Zr ranging from 0.1 to 15.8 ppm, (average = 2.35 ppm), and U from 0.03 to 0.85 ppm (average = 0.23 ppm).

In addition, the different stages of cassiterites for ore-forming process show quite distinctive trace element characteristics. Trace elements in the early-stage sample (WM-8) shows relatively lower concentrations of W (1.3–3636 ppm, average = 503 ppm), but higher concentrations of Sc

(0.5–182 ppm, average = 41 ppm), Ti (23.7–1894 ppm, average = 451 ppm) and V (0.3–210 ppm, average = 43 ppm) compared to the late stage samples (WM-7, MD1901; W: 1.2–7603 ppm, average = 1427 ppm; Sc: 0.2–53 ppm, average = 12.9 ppm; Ti: 0–1269 ppm, average = 246 ppm; V: 0.15–231 ppm, average = 15 ppm). Moreover, general positive correlations can be observed in element pairs of Al and Ga for the whole mineralization stage. The W vs U, Sc vs V and Fe vs Ga only display positive correlations in the early stage, but show no correlation or weak correlation in late mineralization stage (Fig. 11).

## 7. Discussion

### 7.1. Early Cretaceous magmatism and Sn-Cu mineralization under slab roll-back setting

The rock-forming age of the Maodeng Sn-Cu deposit has been debated since it was discovered in 1984. The first bulk rock Rb-Sr isochron age for the causative granite porphyry was reported to be ~149 Ma (Liu, 1996a), although this was only mentioned in the paper with no data. Later, an  $^{40}\text{Ar}-^{39}\text{Ar}$  age of biotite from the porphyritic granite of the Alubaogeshan complex was reported to be  $216.6 \pm 1.6$  Ma (Nie et al., 2007). The zircon U-Pb age of the granite porphyry obtained in this study is  $134.6 \pm 0.7$  Ma, close to the age ( $138.0 \pm 0.6$  Ma) reported by Ji et al. (2021a), but slightly younger than the zircon U-Pb age ( $140 \pm 0.9$  Ma) of the porphyry monzogranite (Ji et al., 2021b) and zircon U-Pb age ( $140 \pm 0.5$  Ma) of the alkali feldspar granite (Ji et al., 2022) of the Alubaogeshan complex, showing the evolution of magma

**Table 1**

LA-ICP-MS trace element compositions (ppm) of zircon from the Maodeng Sn-Cu deposit.

Spot °	Mg ppm	Al ppm	P ppm	Ca ppm	Sc ppm	Ti ppm	Y ppm	Nb ppm	Ta ppm	W ppm	Pb ppm	Th ppm	U ppm	Hf ppm	Sn ppm	La ppm	Ce ppm	Pr ppm
WM-16-02	0.02	0.13	139	0.0	235	3.37	1170	6.59	2.71	0.03	13.68	190	576	11,362	0.00	0.01	14.48	0.10
WM-16-03	0.02	0.23	1857	67.2	254	5.53	772	2.48	1.25	0.03	6.86	121	277	9916	0.00	0.01	14.53	0.12
WM-16-04	0.01	0.11	165	37.2	240	3.87	1022	4.89	2.26	0.03	13.14	192	547	10,791	0.05	0.11	18.42	0.14
WM-16-05	0.00	0.22	139	0.0	239	3.42	858	4.79	2.16	0.02	10.92	149	460	11,154	0.04	0.00	14.08	0.07
WM-16-06	0.09	9.72	168	9.2	249	4.72	741	2.82	1.42	0.03	8.52	132	345	10,946	0.06	0.04	16.88	0.08
WM-16-07	0.01	0.20	145	0.0	241	4.92	915	4.52	2.09	0.02	9.82	154	399	10,500	0.02	0.00	13.92	0.10
WM-16-08	0.00	5.92	111	0.0	245	5.55	1105	2.24	0.74	0.02	4.97	95	203	9622	0.01	0.03	8.57	0.11
WM-16-09	0.50	0.40	127	0.0	235	3.47	802	4.82	2.13	0.06	10.16	136	419	11,299	0.80	0.02	13.62	0.06
WM-16-10	0.08	0.00	132	0.0	236	4.31	975	5.14	2.10	0.01	10.44	156	428	10,731	0.04	0.00	14.32	0.09
WM-16-11	0.00	0.23	175	35.4	255	8.64	563	1.39	0.63	0.02	3.44	60	140	9430	0.02	0.01	8.64	0.06
WM-16-12	0.01	0.22	152	0.0	234	3.18	1029	6.24	2.54	0.06	13.12	188	554	11,343	0.01	0.05	15.23	0.11
WM-16-13	0.00	0.28	187	38.8	251	4.71	651	1.96	1.06	0.01	5.54	91	226	10,417	0.01	0.17	13.25	0.14
WM-16-14	0.25	10.64	132	36.5	230	4.21	939	6.22	2.71	0.17	12.70	167	541	11,637	0.05	0.24	13.42	0.16
WM-16-16	0.20	0.35	178	53.9	246	6.24	808	3.96	1.61	0.02	8.40	136	352	10,044	0.04	0.00	11.80	0.09
WM-16-17	0.00	0.36	162	67.7	256	7.98	525	1.26	0.58	0.01	3.04	52	125	9438	0.06	0.00	7.56	0.05
WM-16-18	0.01	8.00	163	16.7	267	16.46	382	0.74	0.28	0.00	1.59	26	62	8035	0.00	0.00	2.66	0.06
WM-16-20	0.11	43.01	197	51.1	254.8	8.43	608	1.46	0.69	0.07	3.58	63	147	9394	0.05	0.17	9.07	0.11
WM-16-22	0.00	0.31	178	72.9	251.2	6.34	606	1.63	0.79	0.01	4.09	65	170	9608	0.03	0.16	9.22	0.12
WM-16-25	0.06	0.77	170	36.5	226.5	3.09	1145	6.93	2.81	0.08	14.86	220	621	10,987	0.06	0.05	15.81	0.10
WM-16-27	0.16	1.97	200	60.5	226.2	2.77	1727	14.45	5.26	0.08	25.19	346	1066	12,003	0.00	0.10	19.10	0.15
WM-16-30	0.00	12.59	175	110.0	247.9	7.90	1319	1.70	0.78	0.05	6.60	143	267	9696	0.04	0.10	12.07	0.23
Spot	Nd ppm	Sm ppm	Eu ppm	Gd ppm	Tb ppm	Dy ppm	Ho ppm	Er ppm	Tm ppm	Yb ppm	Lu ppm	REE ppm	LREE ppm	HREE ppm	T °C	Th/U	Eu <sub>N</sub> /Eu <sub>N</sub> *	Ce <sub>N</sub> /Ce <sub>N</sub> *
WM-16-02	2.08	5.25	0.01	30.8	10.3	115	40.8	163	33.9	295	49.4	761	21.9	739	681	0.33	0.00	96.4
WM-16-03	2.06	4.68	0.14	23.0	7.3	78	27.4	109	23.1	211	37.3	538	21.5	517	724	0.44	0.04	101.1
WM-16-04	2.19	5.26	0.06	27.1	8.9	100	35.6	144	30.2	267	47.0	686	26.2	660	693	0.35	0.01	37.0
WM-16-05	1.61	3.95	0.02	22.7	7.6	86	30.6	123	26.3	233	39.7	589	19.7	569	683	0.32	0.01	271.3
WM-16-06	1.63	3.94	0.10	20.2	6.6	74	26.1	107	23.0	207	36.1	522	22.7	500	710	0.38	0.03	73.2
WM-16-07	2.28	5.21	0.04	27.1	8.5	94	32.8	129	27.3	244	41.8	626	21.6	605	714	0.39	0.01	193.1
WM-16-08	2.61	6.52	0.13	34.9	10.6	113	38.6	151	30.5	272	46.7	715	18.0	697	724	0.47	0.03	33.2
WM-16-09	1.33	3.62	0.02	21.4	6.9	80	28.4	116	24.4	217	37.2	550	18.7	532	684	0.32	0.01	96.2
WM-16-10	2.27	5.14	0.02	27.5	8.9	98	34.4	138	28.8	254	43.7	655	21.8	633	702	0.36	0.01	185.4
WM-16-11	1.34	3.19	0.22	17.0	5.3	58	20.1	80	16.9	153	27.0	391	13.5	377	766	0.43	0.09	109.7
WM-16-12	1.94	4.69	0.02	27.4	9.2	103	36.3	147	31.0	267	45.8	689	22.0	667	677	0.34	0.01	51.7
WM-16-13	1.62	3.71	0.15	18.6	6.0	66	23.1	94	20.3	182	32.3	461	19.1	442	710	0.40	0.05	20.3
WM-16-14	1.91	4.29	0.04	23.8	8.2	94	33.4	134	28.1	247	41.2	630	20.1	610	700	0.31	0.01	16.6
WM-16-16	1.76	4.39	0.15	23.7	7.5	83	29.1	117	24.8	219	37.4	559	18.2	540	735	0.39	0.04	138.0
WM-16-17	1.33	2.85	0.21	15.4	4.8	54	18.9	75	16.3	147	25.6	369	12.0	357	758	0.42	0.10	163.3
WM-16-18	1.15	2.37	0.35	12.6	3.7	41	13.8	55	11.8	106	19.1	270	6.6	264	833	0.42	0.20	62.5
WM-16-20	1.72	3.71	0.25	18.5	5.7	63	21.7	87	18.4	167	28.8	424	15.0	409	763	0.43	0.09	15.6
WM-16-22	1.64	3.57	0.20	18.0	5.7	62	21.7	87	18.6	172	29.6	430	14.9	415	737	0.38	0.08	16.0
WM-16-25	2.17	5.82	0.02	30.3	10.2	115	40.4	161	33.8	292	49.3	755	24.0	731	674	0.35	0.00	54.6
WM-16-27	2.47	6.68	0.01	41.7	14.7	171	60.8	242	49.7	418	67.2	1094	28.5	1065	665	0.32	0.00	36.3
WM-16-30	4.44	9.62	0.47	45.0	13.2	138	46.6	179	36.5	318	54.0	857	26.9	830	757	0.54	0.07	19.0

chamber. Moreover, LA-ICP-MS U-Pb ages of cassiterites obtained in this study yield lower intercept ages ranging from  $140.0 \pm 6.0$  Ma to  $137.0 \pm 6.0$  Ma, similar to cassiterite U-Pb ages of the cassiterite-sulfide ores from the Maodeng deposit ( $139 \pm 3.2$  Ma) (Ji et al., 2021a) and the nearby Xiaogushan deposit ( $140 \pm 20$  Ma) (Guo et al., 2019). These ages

suggest that the Maodeng Sn-Cu mineralization occurred in the Early Cretaceous (Fig. 7).

In addition to the Maodeng deposit, the coevally Dajing alkali granitic pluton (SHRIMP zircon U-Pb age of  $146.0 \pm 3.7$  Ma) in SGXR hosts large-scale Sn-Cu mineralization (cassiterite U-Pb age of  $144.0 \pm$

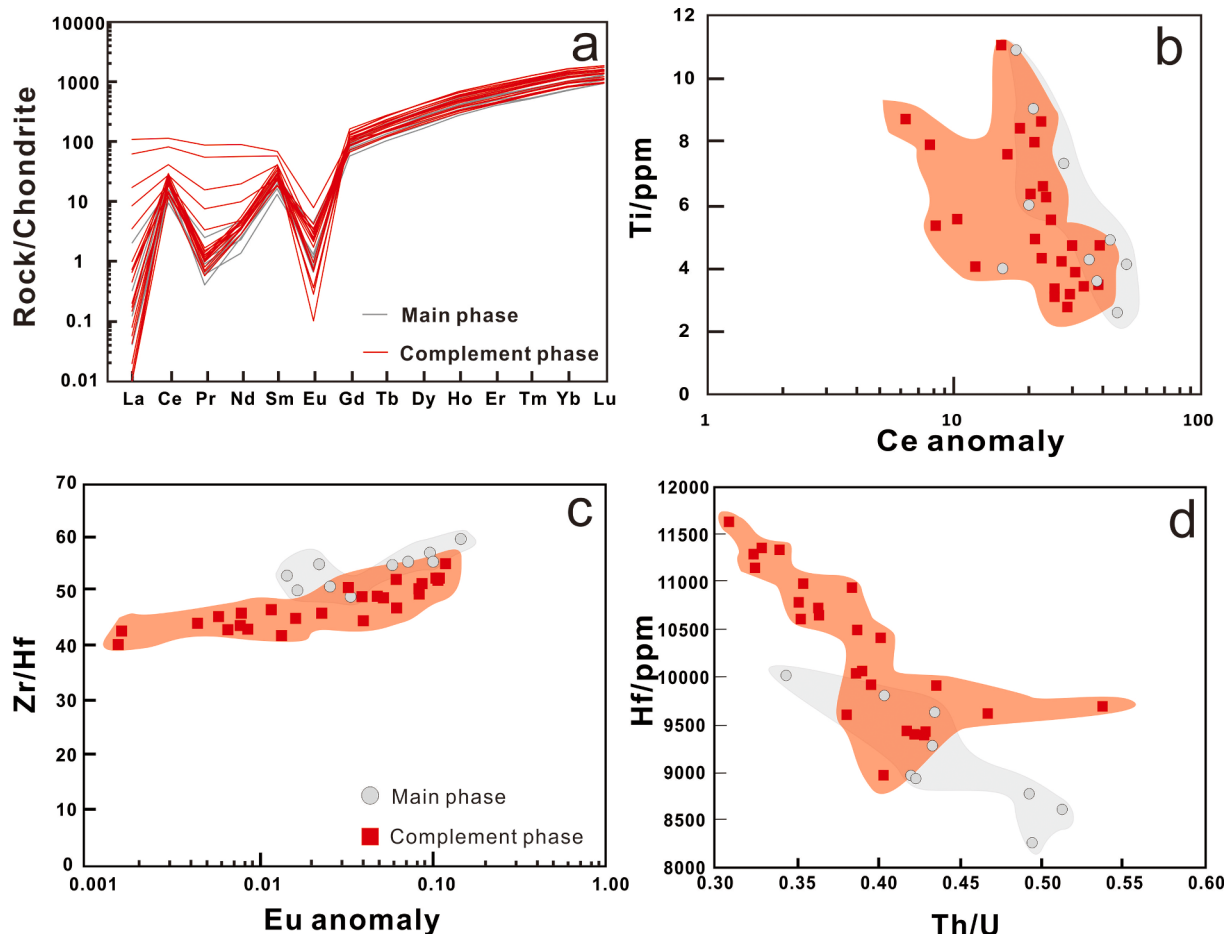


**Fig. 6.** Compositional variations in zircons from porphyry monzogranite (main phase) and granite porphyry (complementary phase). The data of porphyry monzogranite came from Ji et al., 2021b. (a) The normalized chondrite model for zircon REEs in granite porphyry and porphyry monzogranite (chondrite normalized data cited from Sun and McDonough, 1989). (b) plot of Ce anomaly vs Ti. (c) plot of Eu anomaly vs Zr/Hf. (d) plot of Th/U vs Hf.

16 Ma) (Liao et al., 2014). Moreover, the metaluminous Yuanlinzi granitic plutons (zircon U-Pb ages range from  $145.3 \pm 0.5$  Ma to  $141.9 \pm 1.3$  Ma) also contain significant Sn-Cu mineralization (Zhou and Mao, 2022). The chronological data of these tin-copper deposits indicate that they were formed in the same era as the regional tin polymetallic deposits (149–130 Ma; Mao et al., 2019b), showing that the Early Cretaceous is the peak period of ore mineralization in SGXR.

The formation of the Sn deposit is commonly restricted to specific tectonic settings. Lehmann et al. (1990) concluded three types of tectonic setting for ore formation, these are post-collision (e.g., Carboniferous-Permian Sn ore belt in the West Europe), intracontinental arc of the continental margin (e.g., the Tertiary Sn ore belt in Bolivia), and intracontinental extension and rifting (e.g., Cretaceous Sn-W deposits in South China). Voluminous magmatism and associated tin-polymetallic mineralization in the Early Cretaceous (ca. 145–135 Ma) were coeval with the peak of subduction of the Paleo-Pacific plate in a setting of continental margin back-arc spreading and extension of the SGXR (e.g., Zhou et al., 2012; Ouyang et al., 2013; Mao et al., 2019b). Large scale upwelling of the asthenosphere, lithospheric thinning was triggered and thus resulted in the anorogenic magmatism (Wu et al., 2011; Xu et al., 2013), mineralization (Ouyang et al., 2015; Zhou and Mao, 2022) and tectonic activation (Wang et al., 2011, 2015; Wilde and Zhou, 2015; Li et al., 2017a, 2017b) in the SGXR. Furthermore, the eastward shrinking of extents of magmatic activities, together with the progressively younger age from west to east of the volcanic rocks in the SGXR, revealing the roll-back process of the Paleo-Pacific plate (Xu et al., 2019). Because of roll-back of the oceanic slab during subduction,

additional heat and metal elements could be brought from the mantle into the crust during asthenosphere upwelling, resulting in the breakdown of micas in the metasedimentary crust and release of tin (Wolf et al., 2018; Zhao et al., 2022b, 2022c) or the melting of Sn-rich metasedimentary (Wang et al., 2005). The low-pressure characteristics in the extensional background contributes to the formation of melt with small volume percentage and high temperature, which could not be diluted by the materials with low tin contents or low temperature, leading to the formation of melt with high tin mineralization (Wolf et al., 2018; Zhou and Mao, 2022). Meanwhile, partial melting led by dehydration of micas at high temperature is beneficial to tin enrichment in the silicate melt (Yuan et al., 2019; Zhao et al., 2022b). The high heat flux caused by subduction slab roll-back can be used as a deep response to explain the tectonic genesis of SGXR tin deposit province. On the other hand, the strong tectonic regime transformation also activated the tectonic and migration channels, which was more conducive to the upward migration of ore-bearing magmas. Specifically, numerous large tin deposits in the SGXR are all close to deep faults (e.g., Huanggang-Ganzhu'ermao fault), which is favorable to fluids transport under this tectonic setting.

## 7.2. Key factors that control the formation of Sn-Cu mineralization

Magma source, redox state and degree of fractionation of the magmas are petrogenetic factors that control the development of their metal-fertility and sulfur accessibility, and which lead to the formation of magmatic-hydrothermal deposits (e.g., Lehmann, 1990, 2021; Blevin et al., 1996; Sun et al., 2015; Mao et al., 2019b; Sillitoe and Lehmann,

**Table 2**

LA-ICP-MS trace element compositions (ppm) of cassiterite from the Maodeng Sn-Cu deposit.

Spot	Al ppm	Si ppm	P ppm	Sc ppm	Ti ppm	V ppm	Fe ppm	Ni ppm	Ga ppm	Zr ppm	Hf ppm	Nb ppm	Ta ppm	In ppm	Sb ppm	Gd ppm	Tb ppm	W ppm	U ppm	Zr/Hf	Nb/Ta
<b>WM-8</b>																					
WM-8-1	84.2	379	7.02	59.6	3788	83.9	1017	973	9.18	10.53	0.21	0.20	0.02	2458	2.33	17.29	0.46	10.7	0.05	49.48	13.24
WM-8-2	176.1	348	6.17	65.8	1418	50.4	2366	964	21.17	2.22	0.12	0.03	0.02	2396	3.62	17.42	0.51	11.2	0.17		
WM-8-3	20.5	311	6.56	1.1	158	0.8	298	974	1.40	0.45	0.25	0.03	0.02	2428	1.98	16.70	0.48	1270.5	0.48	7.66	
WM-8-4	111.6		6.94	18.1	51	10.3	1071	1011	8.58	0.21	0.01	0.00	0.02	2445	2.02	16.88	0.54	7.2	0.05	2.49	
WM-8-5	213.9	310	7.78	10.9	47	3.5	1775	980	15.17					2421	2.35	17.25	0.48	266.3	0.12		
WM-8-6	184.0	311	8.36	9.2	211	8.9	1579	979	12.66	0.28				2398	2.17	16.58	0.47	133.0	0.05		
WM-8-7	21.5	353	7.09	140.5	812	210.2	457	967	2.11	1.77		0.35		2355	2.77	17.16	0.47	5.9	0.07		
WM-8-8	125.9	315	7.22	53.3	2271	58.9	2001	971	15.02	3.03		0.34		2358	2.75	16.64	0.52	64.6	0.12		
WM-8-9	329.3	290	9.02	15.2	90	2.9	3107	956	27.46	0.10		0.07		2333	3.14	16.96	0.46	2518.9	0.32		
WM-8-10	143.6	279	6.73	69.9	80	8.4	1250	928	12.21	0.29		0.05		2346	1.60	16.55	0.43	142.2	0.08		
WM-8-12	148.3	310	7.98	60.0	1656	51.1	2284	903	17.60	2.53	0.06	0.11		2240	2.93	15.74	0.49	14.8	0.12	45.72	
WM-8-13	8.7	379	7.14	0.6	98	1.2	211	912	0.47	0.15		0.06		2226	2.50	15.38	0.49	774.9	0.65		
WM-8-14	64.3	355	6.80	13.5	299	7.2	1012	957	6.17	1.47		0.01		2242	2.08	16.70	0.49	14.0	0.03		
WM-8-15	133.5	294	8.48	19.9	88	2.2	1858	930	12.95	0.10		0.03		2234	2.55	16.13	0.45	5.9	0.06		
WM-8-16	194.0	265	6.28	28.4	932	25.5	2886	920	21.92	0.85		0.09		2202	3.77	15.00	0.49	13.6	0.11		
WM-8-17	244.2	289	6.37	9.3	47	3.4	2525	919	20.32	0.16		0.02		2199	3.15	15.86	0.49	18.2	0.13		
WM-8-18	57.5		4.95	3.4	624	11.4	336	902	1.02	1.22		1.47	0.02	2184	3.92	15.84	0.49	1433.8	0.70	70.43	
WM-8-19	81.2	307	5.80	71.8	948	75.7	1608	898	8.12	1.21		0.07		2162	2.65	16.21	0.47	1.3	0.07		
WM-8-20	10.2	288	7.20	1.0	409	1.4	313	895	0.73	0.54	0.03	0.61	0.01	2136	3.41	14.90	0.49	1963.4	0.28	20.66	71.62
WM-8-21	8.4	304	7.61	0.7	61	0.9	219	885	0.52	0.11		0.05		2103	2.87	15.32	0.44	536.7	0.58		
Spot	Al ppm	Si ppm	P ppm	Sc ppm	Ti ppm	V ppm	Fe ppm	Ni ppm	Ga ppm	Zr ppm	Hf ppm	Nb ppm	Ta ppm	In ppm	Sb ppm	Gd ppm	Tb ppm	W ppm	U ppm	Zr/Hf	Nb/Ta
11 WM-8-22	9.1	260	6.87	0.5	112	0.3	268	882	0.37	0.19	0.10			2108	2.15	15.05	0.49	1661.7	0.38		
WM-8-23	14.3	347	7.08	3.5	2493	4.1	411	883	0.99	3.64	0.10	4.40	0.04	2047	3.97	13.96	0.48	3636.6	0.77	37.27	99.00
WM-8-24	31.9	297	6.58	121.7	2345	189.8	653	866	3.15	6.99	0.06	1.19	0.01	2029	2.69	14.66	0.39	14.4	0.37	124.40	108.39
WM-8-25	26.5	296	7.17	182.1	603	163.4	588	869	2.70	2.05		0.32	0.01	2084	1.98	14.69	0.42	9.6	0.08		48.44
WM-8-26	87.4	364	6.45	74.5	619	78.8	1874	867	8.64	0.66		0.04		2054	1.52	14.24	0.47	1.6	0.07		
WM-8-27	79.4	364	7.83	68.4	3322	122.3	1733	848	9.68	7.08	0.07	0.26		2016	1.81	13.95	0.44	7.3	0.08		105.37
WM-8-28	122.6	265	5.40	31.8	547	33.0	2304	870	13.16	1.46		0.18		2034	1.76	13.93	0.47	9.6	0.14		
WM-8-29	109.5	263	5.80	49.4	1979	36.2	2248	847	12.70	2.91		0.27		2005	1.40	14.02	0.36	11.4	0.05		
WM-8-30	244.4	278	6.27	19.7	57	1.6	3358	868	21.01					2024	2.42	13.68	0.50	28.4	0.16		
<b>WM-7</b>																					
WM-7-1	6.8	486	6.95	0.4	278	4.6	246	940	0.39	0.41		0.01	0.01	2275	0.83	16.79	0.49	1475.0	0.43		1.69
WM-7-2	8.1	291	8.06	0.6	946	1.4	265	937	0.63	1.77	0.03	0.22		2280	0.59	15.83	0.51	2546.8	0.31	61.79	
WM-7-3	51.7	304	7.85	4.3	2537	9.9	980	935	4.76	15.82	0.26	11.43	0.07	2243	1.91	15.34	0.45	7257.7	0.28	61.04	166.00
WM-7-4	167.6		7.32	6.2		0.3	2630	965	23.26					2284	3.99	17.17	0.45	13.7	0.07		
WM-7-5	52.8	341	8.54	17.4	741	26.4	1055	961	2.14	0.75		0.01		2284	1.78	16.23	0.49	32.3	0.12		
WM-7-7	157.7	359	5.0	74	4.4	2302	956	7.89			0.01			2326	3.13	16.94	0.60	25.3	0.11		
WM-7-8	6.1		5.68	0.6	180	0.2	308	962	0.56	0.55		0.11		2262	4.54	16.45	0.48	2824.4	0.39		
WM-7-9	5.2	272	7.84	0.9	288	0.9	254	965	0.36	0.57		0.14		2285	3.48	16.38	0.49	799.6	0.62		
WM-7-10	6.7	399	6.72	1.2	351	0.6	391	968	0.71	1.04		0.29		2317	3.25	16.43	0.58	3765.3	0.39		
WM-7-11	86.2	393	7.90	4.2	257	1.3	1478	997	8.31	0.55		0.09		2355	2.87	16.76	0.48	1505.2	0.41		
WM-7-12	112.9	404	8.12	17.0	492	16.5	2801	1001	8.30	1.29	0.02	0.05		2402	3.42	17.28	0.47	38.3	0.11	66.07	
WM-7-13	90.6	374	7.59	3.0	9	0.4	2204	1004	8.41					2402	3.46	16.94	0.51	5.2	0.06		
WM-7-14	18.7	351	8.29	2.5	20	8.2	421	991	1.33					2372	2.37	15.78	0.50	128.5	0.06		
Spot	Al ppm	Si ppm	P ppm	Sc ppm	Ti ppm	V ppm	Fe ppm	Ni ppm	Ga ppm	Zr ppm	Hf ppm	Nb ppm	Ta ppm	In ppm	Sb ppm	Gd ppm	Tb ppm	W ppm	U ppm	Zr/Hf	Nb/Ta
WM-7-15	147.9	414	7.33	1.9	82	1.5	3248	1008	10.08					2424	5.50	17.30	0.45	915.9	0.14		
WM-7-16	288.6	326	8.16	6.4	490	8.9	4530	991	15.89	1.68		0.05		2437	5.12	17.80	0.48	1870.5	0.13		
WM-7-17	107.5	422	8.60	43.4	850	92.3	2314	1007	12.53	2.58		0.01		2451	3.35	17.05	0.57	15.0	0.06		
WM-7-18	143.1	461	7.22	44.5	683	15.6	5133	1030	3.97	4.17	0.14	0.13	0.01	2455	7.06	16.87	0.48	14.4	0.76	30.04	16.43
WM-7-19	43.5	371	7.53	20.7	2039	12.5	1728	1010	1.48	4.34	0.04	2.30	0.06	2426	4.96	16.89	0.54	444.1	0.33	97.42	35.74

(continued on next page)

**Table 2 (continued)**

Spot	Al ppm	Si ppm	P ppm	Sc ppm	Ti ppm	V ppm	Fe ppm	Ni ppm	Ga ppm	Zr ppm	Hf ppm	Nb ppm	Ta ppm	In ppm	Sb ppm	Gd ppm	Tb ppm	W ppm	U ppm	Zr/Hf	Nb/Ta
Spot	Al ppm	Si ppm	P ppm	Sc ppm	Ti ppm	V ppm	Fe ppm	Ni ppm	Ga ppm	Zr ppm	Hf ppm	Nb ppm	Ta ppm	In ppm	Sb ppm	Gd ppm	Tb ppm	W ppm	U ppm	Zr/Hf	Nb/Ta
WM-7-20	8.2	371	7.02	0.2		0.2	383	1044	0.64			0.01	0.01	2489	4.44	16.79	0.59	1517.5	0.42		1.08
WM-7-21	12.3	471	6.56			0.2	229	1038	1.03					2702	4.47	18.73	0.56	2482.1	0.31		
WM-7-22	8.1	415	7.52	0.3		0.2	228	1036	0.67	0.10		0.01		2653	3.22	18.03	0.64	2349.4	0.09		
WM-7-23	163.3	398	8.05	14.7	615	5.8	1802	1043	19.74	3.61		0.07		2630	3.40	18.13	0.60	138.4	0.28		
WM-7-24	70.6	385	8.15	21.1	281	9.2	905	1065	7.30	0.80		0.01		2624	2.41	17.70	0.61	33.1	0.05		
WM-7-25	194.7	493	7.12	4.3			2091	1048	20.66					2626	3.38	16.91	0.54	134.7	0.29		
WM-7-26	104.4	394	6.28	6.6	16	2.9	1593	1036	9.76					2605	2.28	17.98	0.53	32.9	0.10		
WM-7-27	5.6	373	8.58	0.3	295	1.8	209	1050	0.44	0.60		0.05		2592	3.50	17.78	0.48	2138.8	0.44		
WM-7-28	18.6	354	8.35	0.7	170	0.4	434	1056	1.88	0.58		0.23	0.01	2570	3.36	17.72	0.48	6394.6	0.34		26.95
WM-7-29	178.0	303	8.00	21.1	1067	47.8	1598	1010	16.28	4.77	0.09	0.11		2509	3.10	17.79	0.47	9.1	0.11	53.28	
<b>MD1901</b>																					
MD1901-1	194.8	363	7.58	7.1	233	13.9	1898	997	12.78	0.62				2529	3.37	18.35	0.45	41.0	0.07		
MD1901-2	166.8		6.49	52.1	1203	231.9	2064	994	16.56	11.75	0.32	0.12		2499	2.74	17.40	0.54	19.3	0.09	36.32	
MD1901-3	110.9	335	8.48	15.9	185	12.4	1752	1003	8.15	0.40		0.04		2510	2.12	18.23	0.48	2.8	0.05		
MD1901-4	116.4	356	8.55	20.2	260	12.4	2318	1000	10.47	1.08		0.04	0.00	2472	3.07	17.82	0.56	4.3	0.10	10.05	
MD1901-5	125.3	378	7.02	10.2	79	4.2	2059	1005	11.40	0.35				2428	2.68	17.54	0.55	13.3	0.12		
MD1901-6	251.2	376	7.02	28.9	370	2.5	3548	1003	27.81	1.52		0.04		2442	2.51	17.61	0.56	24.2	0.26		
MD1901-7	15.5		8.20	1.9	210	0.6	539	995	1.50	2.29	0.03	1.30	0.02	2381	4.02	16.80	0.56	5572.4	0.16	73.96	74.12
<b>Spot</b>																					
MD1901-8	8.3		7.47	2.6	514	2.0	413	980	0.97	2.23		0.61		2371	2.72	16.75	0.55	4032.3	0.11		
MD1901-9	134.4	353	7.89	28.1	474	9.6	1791	978	15.17	1.30		0.08		2382	2.14	16.47	0.47	318.8	0.13		
MD1901-10	9.6	312	7.55	0.8	1605	4.7	329	964	0.61	5.42	0.05	3.27		2353	1.72	17.14	0.58	3556.4	0.44	109.19	
MD1901-11	25.6	286	7.42	0.8	139	0.4	756	946	2.15	1.10	0.02	0.54	0.01	2318	2.38	16.24	0.47	7603.0	0.18	44.99	39.03
MD1901-12	4.9	259	8.38	1.9	1452	1.5	330	933	0.15	6.80	0.22	4.27	0.13	2301	2.09	17.06	0.46	3292.7	0.85	31.19	32.21
MD1901-13	116.8	392	6.95	11.4	267	6.3	2129	971	11.22	1.25	0.05	0.06		2331	2.00	16.12	0.46	25.1	0.11	24.35	
MD1901-14	171.8	391	7.31	14.3	302	11.6	2013	948	16.95	0.79		0.02		2285	2.29	16.32	0.54	277.2	0.20		
MD1901-15	79.0	391	6.67	53.4	206	24.7	1331	979	8.23	0.50				2289	2.19	16.31	0.51	1.2	0.03		
MD1901-16	74.5	332	6.64	42.3	874	54.9	1301	953	8.08	2.28				2297	1.93	16.04	0.52	3.9	0.07		
MD1901-17	11.8	351	6.62	0.9	247	0.8	302	946	0.98	1.37		0.09		2272	2.31	15.94	0.53	2569.7	0.48		
MD1901-18	152.6	327	6.38	14.5	521	8.1	2267	950	19.17	3.75	0.06	0.07		2278	1.48	16.62	0.52	82.2	0.12	60.07	
MD1901-19	14.1	332	7.35	1.1	834	0.5	334	951	0.89	8.60	0.21	1.07	0.01	2257	2.23	16.19	0.57	2660.2	0.32	41.34	107.00
MD1901-20	113.8	333	9.97	46.5	890	27.7	1538	947	12.89	3.25	0.04	0.07		2264	2.98	16.87	0.48	9.2	0.11	74.61	

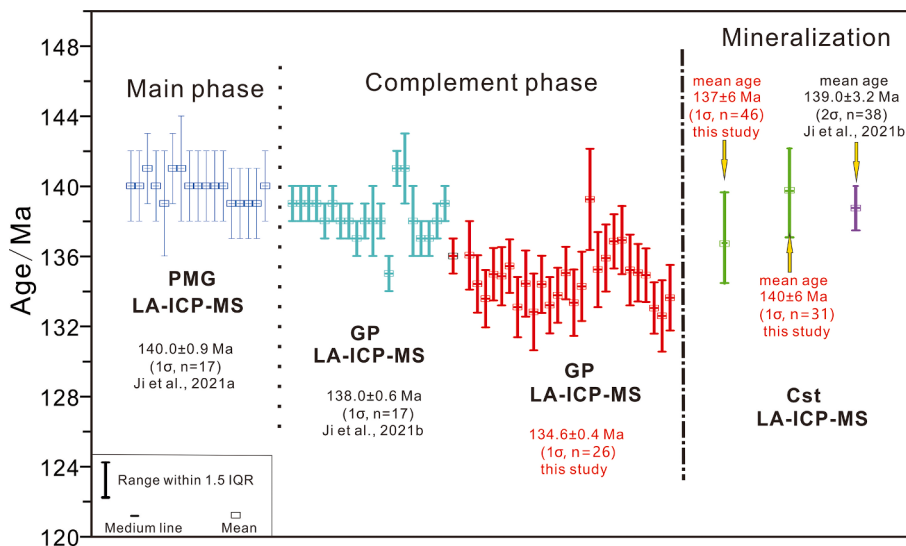


**Fig. 7.** Geological time frame of the Maodeng Sn-Cu deposit is constrained by crosscutting relationships and geochronology. See text for detailed discussion. Compiled chronological data in grey are from previous studies (Guo et al., 2019; Ji et al., 2021b; Liu et al., 2018; Cheng et al., 2014). Abbreviations: GP = granite porphyry, PMG = porphyry monzogranite, Cst = cassiterite.

2022). Owing to the highly incompatible behaviour, Sn is enriched in the continental crust and highly evolved granitic magmas derived from the partial melting of metapelites rocks (Lehmann, 2021; Gardiner et al., 2017). In addition, Cu (-Au) is interpreted to be associated with the more mafic end of the granite spectrum, and Sn (-W) with more felsic and fractionated granites (Blevin, 2004). Magma oxidation states also provide strong constraints on the ore element assemblages, with the Cu-Mo-Au series associated with oxidized granites (magnetite series), and Sn with reduced granites (ilmenite series) (Ishihara, 1981; Blevin, 2004).

#### 7.2.1. Degree of magmatic fractionation in the Maodeng ore field

The fractional crystallization indices, including bulk-rock SiO<sub>2</sub> and Nb/Ta, Zr/Hf, and Rb/Sr ratios, are commonly applied to evaluate the degree of magma fractionation (Lehmann, 1990; Ballouard et al., 2016). In terms of the geochemical characteristics of bulk-rock (e.g., Cheng et al., 2014; Guo et al., 2019; Ji et al., 2021b), the granite porphyry (complement phase) has the higher SiO<sub>2</sub> contents (71.5–77.4 wt%) and Rb/Sr ratios (3.39–10.33), as well as lower MgO (0.12–0.46 wt%), Sr (21–54 ppm), Ba (97–276 ppm) contents and Nb/Ta ratios (10.86–13.06) than those of the porphyry monzogranite (main phase) (SiO<sub>2</sub>, MgO, Sr, Ba contents of 70.4–72.1 wt%, 0.26–0.47 wt%, 120–167 ppm, and 467–649 ppm, respectively; Rb/Sr and Nb/Ta ratios of 1.03–1.72 and 13.34–15.83, respectively), reflect the highly fractionated nature of granite porphyry (Fig. 8a). In addition, trace elements of zircons are robust indicators for magma evolution (Hoskin and Schaltegger, 2003; Gardiner et al., 2017), and the characteristics of parent magma thus can be reliably described (Li et al., 2021a, 2021b). Compared to the main phase (PMG), the complement phase (GP) displays more evolved signatures with relatively high Hf contents, but low Eu<sub>N</sub>/Eu<sub>N</sub><sup>\*</sup>, Th/U, and Zr/Hf ratios (Fig. 6). Moreover, Eu<sub>N</sub>/Eu<sub>N</sub><sup>\*</sup> ratios show an overall decrease as Zr/Hf ratios decrease, suggesting a phenomenon of plagioclase/feldspar crystallization, the zircon trace elements in the PMG and GP thus could support the crystal fractionation processes in the district (Deering et al., 2016; Li et al., 2021a, 2021b).

As discussed above, zircons from GP and PMG have consistent U-Pb ages, and previous studies (Ji et al., 2021b, 2022) have also shown that the two granitoids have similar Sr-Nd-Hf isotopes, indicating the same source, i.e., the depleted mantle, for diagenetic materials. In addition, the field contact relationship suggests that there is no obvious boundary between the two granitoids, but a transition contact relationship of phase transformation (Guo et al., 2019). We thus believe that the granite

porphyry may be the results of further fractionation and evolution of porphyry monzogranite, and they are related to the crystallization differentiation of same magma system.

#### 7.2.2. Metallogenetic difference of Sn-Cu and Sn-W deposits in the SGXR

The Sn-W and Sn-Cu related granites are widely developed in the SGXR, however, their geochemical compositions are quite different. The Sn-W associated granites are strongly- to moderately-evolved and fractionated, as shown by their relatively high SiO<sub>2</sub> contents (68.0–80.3 wt %) and Rb/Sr ratios (4.6–408; average = 68), and relatively low Nb/Ta ratios (1.6–195; average = 6.2), Zr/Hf ratios (0.18–19.26; average = 12.29) and Sr contents (3.09–69.20 ppm) (Fig. 8a) (Supplementary Table S2). In contrast, the Sn-Cu related granites are in relatively low degree of fractionation, with the characteristics of relatively low SiO<sub>2</sub> contents (66.6–77.8 wt%) and Rb/Sr ratios (0.3–10.3; average = 3.3), but the Nb/Ta ratios (6.3–15.8; average = 11.4), Zr/Hf ratios (2.94–32.98; average = 19.94) and Sr contents (21–360 ppm) are higher than those of Sn-W associated granites (Supplementary Table S2). These data reflect that the Sn-W associated granites have the higher degree of fractionation than the Sn-Cu related granites.

Several redox indicators, including bulk-rock Fe<sub>2</sub>O<sub>3</sub>/FeO, zircon Ce<sup>4+</sup>/Ce<sup>3+</sup> and Ce<sub>N</sub>/Ce<sub>N</sub><sup>\*</sup> ratios are widely adopted to determine the redox states of the magma (e.g., Ballard et al., 2002; Trail et al., 2011, 2012; Shu et al., 2019). Under reduced conditions (ilmenite-series granites), tin is predominantly divalent and behaves incompatible, tending to enrich in silicate melts, whereas in high oxygen fugacity Sn displays compatible, entering the mineral phase (cassiterite, stannite, Ti-rich minerals) as tetravalent (Lehmann, 1990; Blevin et al., 1996). While copper is a strong chalcophile element, its geochemical behavior is controlled by the valence state and occurrence state of sulfur (Sun et al., 2015). At fairly high fO<sub>2</sub>, sulfur exists mainly in the form of sulfate (Jugo et al., 2005, 2010). Copper shows incompatibility at this time and gradually concentrates in the oxidized melt. Residual sulfides would release sulfophilic elements (e.g., Cu, Au) due to the instability, which make the magmas copper-rich (Yang et al., 2008; Zajacz et al., 2013; Sun et al., 2013, 2020). The Sn-W associated granites are mostly plot in the area of the ilmenite-series granites (Fig. 8b) due to the low Fe<sub>2</sub>O<sub>3</sub>/FeO values (0.01–1.3) and high SiO<sub>2</sub> contents (67.97–80.28 wt%). They have relatively low fO<sub>2</sub> values characterized by the low zircon Ce<sub>N</sub>/Ce<sub>N</sub><sup>\*</sup> (6.99–71.32; average = 35.45) and Eu<sub>N</sub>/Eu<sub>N</sub><sup>\*</sup> (0.004–0.26; average = 0.08) (Fig. 8b-d). By contrast, the Sn-Cu related granites have much

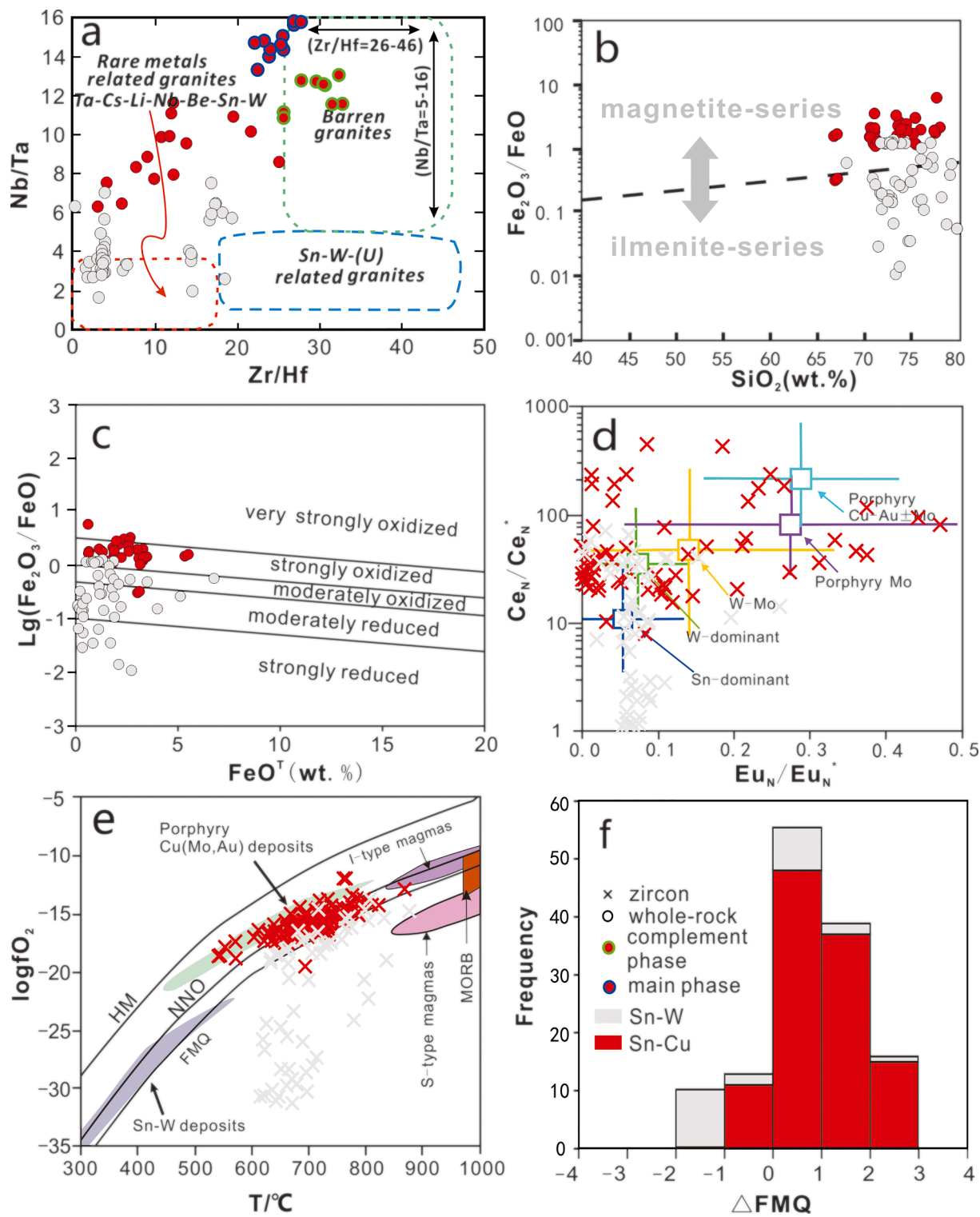


**Fig. 8.** Bulk rock (a-c) and Zircon (d-e) major and trace elements plots of  $f\text{O}_2$  in Maodeng deposit. (a) Zr/Hf vs Nb/Ta diagram; (b) SiO<sub>2</sub> vs Fe<sub>2</sub>O<sub>3</sub>/FeO diagram; (c) FeO<sup>T</sup> vs log (Fe<sub>2</sub>O<sub>3</sub>/FeO) diagram (after Blevin, 2004); (d) Eu<sub>N</sub>/Eu<sub>N</sub><sup>\*</sup> and Ce<sub>N</sub>/Ce<sub>N</sub><sup>\*</sup> (after Niu et al., 2022); (e) T vs logfO<sub>2</sub> (after Richards, 2015); (f)  $\Delta\text{FMQ}$  histogram. Data from: Guo et al., 2019; Ji et al., 2021b; Zhou et al., unpublished data; Jiang et al., 2016; Gao et al., 2019; Wang et al., 2017; Yang et al., 2019; Yao et al., 2017; Liu et al., 2017; Niu et al., 2022.

higher bulk-rock Fe<sub>2</sub>O<sub>3</sub>/FeO values (0.31–5.9), and Ce<sub>N</sub>/Ce<sub>N</sub><sup>\*</sup> (7.94–452.3; average = 74.82) and Eu<sub>N</sub>/Eu<sub>N</sub><sup>\*</sup> (0.002–0.47; average = 0.13) ratios, suggest that they belong to the magnetite-series granites with high  $f\text{O}_2$  (e.g., strongly- to very strongly oxidized) (Fig. 8b-d). The calculated lgfO<sub>2</sub> values based on the trace elements of zircons from the Sn-W granites range from -19.35 to -13.83 (average = -16.82), and

$\Delta\text{FMQ}$  values range from -1.93 to + 2.75 (average = -0.33), further indicating that the Sn-W associated granites are relatively reduced (Fig. 8e-f). While Sn-Cu associated granites are more oxidized as evidenced by the high lgfO<sub>2</sub> values (-17.94 – -12.03; average = -15.9) and  $\Delta\text{FMQ}$  (-0.65 – +3.69; average = +1.19) values (Fig. 8e-f).

In addition, it has been suggested that magmatic rocks with higher

ASI ( $A/CNK > 1.1$ ) have lower Nb/Ta ratios and have higher mineralization potential (Ballouard et al., 2016, 2020; Wu et al., 2017). More recently, Zhao et al. (2022a) have shown that fluids from high-ASI magmas are easier to extract more tin, thereby enriching ore-bearing magmas and/or ore-forming fluids. Ore-forming fluids exsolved from highly fractionated magmas (Sn-W associated granites) can thus sequester enough Sn to form Sn deposits with more reserves than Sn-Cu counterparts (Zhou and Mao, 2022). Furthermore, experimental results indicate that the solubility of Sn in peraluminous granitic magma is strongly controlled by the oxygen fugacity (Taylor and Wall, 1993; Duc-Tin et al., 2007), high  $f_{O_2}$  conditions are not favorable to the formation of tin-bearing granites, nor to the formation of Sn polymetallic deposits (Lehmann, 2021; Yuan et al., 2020). In summary, the potential for ore-forming magmas to produce economic tin mineralization is usually attributed to several factors (Shu et al., 2019), with Sn-W associated granites are more fractionated and more reduced than Sn-Cu granites. Relatively low differentiation degree and high oxygen fugacity of Sn-Cu magma limit the scale of Sn mineralization in Sn-Cu deposits.

#### 7.2.3. Injection of oxidized fluids exsolved from mafic magmas to Sn-Cu-bearing fluids

Protolith lithology is the controlling factor that determines the oxidation state and metal endowments of the magma (Sato, 2012;

Romer and Kroner, 2016; Lehmann, 2021; Sillitoe and Lehmann, 2022). More recently, Sillitoe and Lehmann (2022) proposed that the genesis of Cu-rich Sn deposit was due to the provision of ascendant oxidized magmatic-hydrothermal fluids to reduced, albeit less-fractionated magma chambers. The relatively low initial  $^{87}\text{Sr}/^{86}\text{Sr}$  values (0.7029–0.7045) and high  $\epsilon_{\text{Nd}}(t)$  values (0.8–4.4) indicates the Maodeng Sn-Cu related granites are mainly derived from partial melting of a juvenile lower crust that originated from the depleted mantle (Ji et al., 2021b). Moreover, the Sn-Cu associated granites have higher incompatible elements contents (e.g., V (4.95–44.8 ppm, average = 24.98 ppm), Cr (2.46–27.9 ppm, average = 16.03 ppm), Co (0.19–10.4 ppm, average = 2.77 ppm)) than those in Sn-W associated granites (V (1.11–18 ppm, average = 7.62 ppm), Cr (0.01–18.9 ppm, average = 3.91 ppm), Co (0.03–4.81 ppm, average = 0.73 ppm)) (Guo et al., 2019; Ji et al., 2021b; Zhou et al., unpublished data), suggest the higher mantle materials are involved in the Sn-Cu related granitic magma. In addition, the He-Ar isotopic compositions of ore-forming fluids of Cu-rich tin deposit, for instance, the Dajing Sn-Cu polymetallic deposit, have relatively high  $^3\text{He}/^4\text{He}$  ratios (2.58–3.16 Ra), suggest that the mantle materials involved in mineralization process (Wang et al., 2008), and the analysis on Sr-Nd-Pb-O isotope also shows that granitic magmas and its ore-forming materials are related to crust-mantle interaction process (Shao et al., 2010; Ouyang et al., 2015).

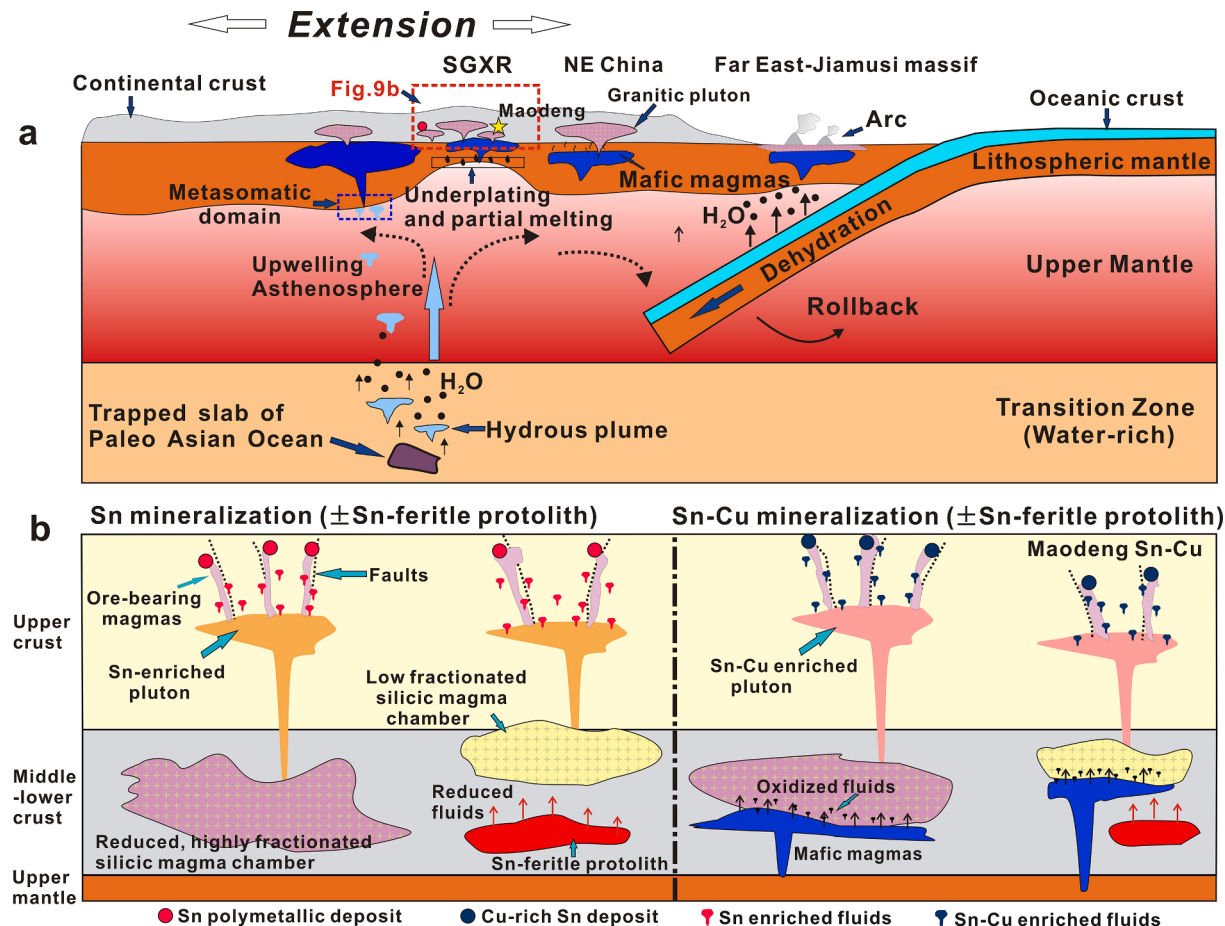


**Fig. 9.** Genetic model of the Maodeng Sn-Cu deposit (modified after Li et al., 2017a, 2017b; Sillitoe and Lehmann, 2022; Harlaux et al., 2021b). (a) The roll-back of the Paleo-Pacific plate leads to the regional extension in SGXR, which is conducive to the asthenosphere upwelling and injection of mantle-derived magma. Meanwhile, it causes large-scale partial melting of crustal materials and the formation of the felsic melts and silicate magma chambers. (b) There are two ways for the formation of tin-rich magma. One is extreme magmatic differentiation, the other is relatively low degree of differentiation but with Sn-ferile protolith. In case of Maodeng, it corresponds to the latter. Furthermore, we emphasize the key role of mantle-derived mafic magmas in forming copper-rich tin deposits. In other words, the injection of mantle-derived magma is the main factor leading to the difference of Sn-polymetallic mineralization. The oxidized fluids exsolved from mantle-derived magmas can introduce copper to the Sn-rich silicic chambers, as a result, making the ore-forming fluids with the fertility for Cu-rich Sn mineralization after further magma mixing and evolution. See detail discussions in text.

Field geological phenomena have always been strong evidence of geological principles (e.g., Zhai et al., 2020; Wu et al., 2020; Li et al., 2021a, 2021b). The mafic microgranular enclaves (MMEs) are ubiquitous in the Maodeng granite porphyry (Fig. 3l), indicating that the mantle-derived melt or fluid may be involved in the formation of the granitic magmas in the Maodeng deposit (Fig. 9). Furthermore, the SGXR are essentially composed of accretionary complexes after the late Paleozoic (Xiao et al., 2009; Wilde, 2015). These stacked sediments were intruded by Mesozoic to Cenozoic magmas from depth under the various tectonic setting. Therefore, significant mixing may have occurred between the deeply generated oxidized magmas and C-bearing accreted sediments during the intrusion and mineralization periods (e.g., Ishihara et al., 2006). In fact, it has been widely proved and accepted that the SGXR had obvious crust-mantle interaction process in the Late Mesozoic; i.e., the development of Early Cretaceous basic swarm dikes, widely developed mafic dikes, and the emergence of overflow basalt, etc., suggest the intense mantle-sourced magmatic activity (Ge et al., 1999; Shao et al., 2005; Li et al., 2017a, 2017b, 2018). A similar example is the world-class San Rafael Sn-Cu deposit, central Andean tin belt, where the mafic rocks (e.g., lamprophyre) are ubiquitous, and the Sn-Cu mineralization was considered to be resulted from lamprophyric magmas mixing with peraluminous S-type biotite-cordierite magmas (hybridization) (Harlaux et al., 2021a, b; Sillitoe and Lehmann, 2022).

### 7.3. Tracing fluids evolution process from the trace element variations in cassiterite

The ease with which trace elements can be incorporated in cassiterite can be estimated from the divergence of their ionic radius, charge balance, and coordination of ions with respect to  $\text{Sn}^{4+}$ , which itself exists in octahedral coordination (Zhou et al., 2022a). There are two valence states of tin under geological conditions, among which the  $\text{Sn}^{2+}$  is 0.93 Å in ionic radius (when coordination number is 6), and the ion radii of  $\text{Sn}^{4+}$  are 0.69 Å and 0.81 Å (when the coordination number is 6 and 8, respectively) (Shannon and Prewitt (1969, 1970)). Tin therefore can be easily substituted with a variety of elements in isomorphism. Based on the ionic radius, charge balance, and the geochemical properties of elements, we consider the following elements likely to be abundant in cassiterites in this study:  $\text{Al}^{3+}$ ,  $\text{Sc}^{3+}$ ,  $\text{Ti}^{4+}$ ,  $\text{V}^{5+}$ ,  $\text{Cr}^{3+}$ ,  $\text{Fe}^{3+}$ ,  $\text{Ga}^{3+}$ ,  $\text{Zr}^{4+}$ ,  $\text{Nb}^{5+}$ ,  $\text{Ta}^{5+}$ ,  $\text{In}^{3+}$ ,  $\text{W}^{4+}$  and  $\text{U}^{4+}$ , which is similar with the anterior

researches (Möller et al. 1988; Guo et al., 2018a, 2018b; Cheng et al., 2019; Mao et al., 2020).

Temperature serves a key controlling factor on compositional variation in cassiterites. Cassiterites formed under high-temperature hydrothermal fluids commonly have high Nb, Ta, Zr and low Fe, Mn contents, while under low temperature would behave the opposite characteristics of the former (Tindle and Breaks, 1998; Zhang et al., 2017; Guo et al., 2018a). The cassiterites from the Maodeng deposit are characterized by low Nb, Ta, and high Fe, Ti contents, indicating the relatively low-temperature forming settings. Hydrogen and oxygen isotopic compositions of the ore-forming fluids from different mineralization stages suggest that the increasing precipitation in meteoric water and fluid cooling process from early to late stage (Liu, 1996a). The continuously decrease in temperature results in the unstable decomposition of the Sn-containing complex and the precipitation of the tin ores. In addition, compared to the early stage, cassiterites in the late stage show higher Zr/Hf and Nb/Ta ratios, which are attributed to the progressive precipitation of incompatible element-enriched minerals (e.g., zircons, rutile) (Wu et al., 2021), or owing to the enrichment of F and/or B in ore-forming fluids (Cheng et al., 2019).

The concentrations of analytical elements varied between the early and the late stage (Fig. 10). Specifically, the cassiterites from the early stage (quartz-cassiterite (-wolframite) stage) contains higher Sc, Ti, V contents compared to those of the late stage (base-metal sulfides stage), while W concentrations increased significantly in the late stage (Fig. 10). Positive correlations of element pairs can only be observed in the early stage (like Sc-V, Fe-Ga) (Fig. 11a-b). Combined with the information provided by fluid inclusions, which show a predominance of  $\text{F}^-$  within the late-stage mineralized fluids, and display a trend of more  $\text{H}_2$  contents and more acidic of ore-forming fluids with evolution (Liu 1996a, b). We try to explain this phenomenon by using the following substitution mechanisms and the variable volatile contents. The strong positive correlation between V and Sc was recognized in the early stage (Fig. 11a), allowing the substitution of  $\text{Sc}^{3+} + \text{V}^{5+} = 2\text{Sn}^{4+}$ . However, none correlation can be observed in the late stage, indicating that there may be caused by external factors as described below. Wang et al. (2022) recently reported the highly coupled between Sc and F at medium and low temperatures through experimental investigation. We propose that it is the high F concentrations in the hydrothermal fluids of late-stage that allowed Sc to be transported out of cassiterites with the

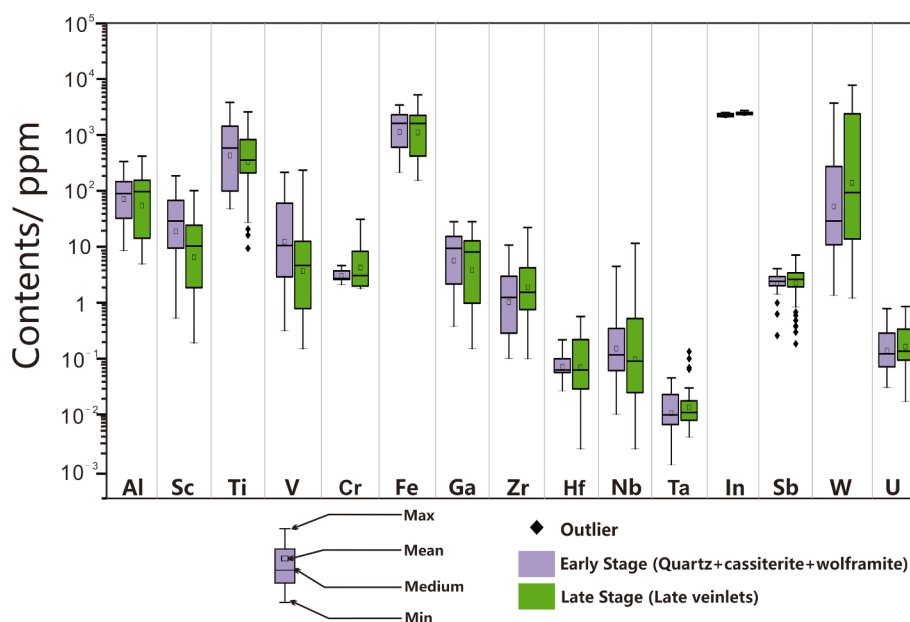


**Fig. 10.** Box-whisker diagrams showing elements investigated in this study and their contents. Most trace element contents are decreased from early to late stages, except for W and U.

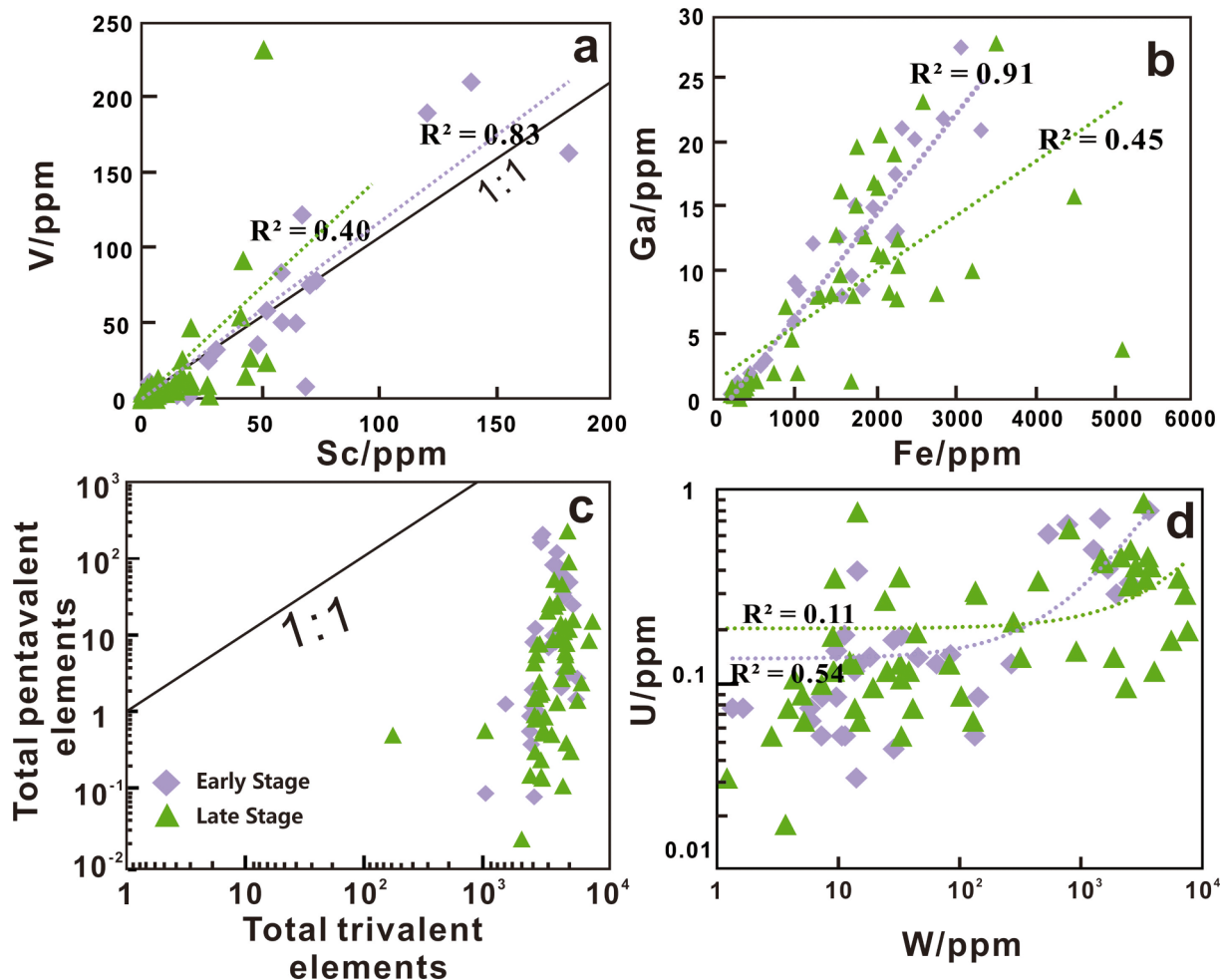
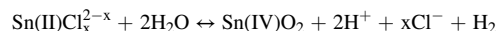


**Fig. 11.** Selected diagrams of trace elements in the cassiterite samples. (a) Sc vs V; (b) Fe vs Ga; (c) total trivalent elements vs total pentavalent elements and (d) W vs U.

fluids, in the form of  $\text{ScF}_2^+$  and/or  $\text{ScF}_3^0$ , result in the lower Sc contents of cassiterites in late stage (Wang et al., 2022). Interestingly, Fe-Ga pair also shows different coupling properties between the early and late mineralization stage (Fig. 11b), differs to Gejiu Sn-Cu deposit (e.g., Cheng et al., 2019), which have been attributed to the acidic evolution of ore-forming fluids (Liu 1996a). Cassiterites from the Maodeng deposit also show much higher trivalent elements concentrations than those of pentavalent elements (Fig. 11c), which is possible to be caused by the presence of  $\text{H}^+$  to balance the charge (Cheng et al., 2019; Mao et al., 2020). We suppose that the addition of  $\text{H}^+$  in the late stage enables the reaction  $\text{Fe}^{3+} + \text{H}^+ \rightarrow \text{Sn}^{4+}$  to occur, and thus makes the Fe-Ga non-correlation. The elemental coupling above thereby successfully supports the conclusions of fluid inclusions.

The W and U are expected to occur as either 4 + or 6 + ions collectively (Cheng et al., 2019), and are both incompatible elements., the similarly geochemical properties of lead to the weak correlation between W and U in the early stage. However, the incompatibility of W is greater than that of U, concentrations of W would become significantly more abundant than U with evolution. In addition, it is worth noting that the sensitivity of W and U to oxygen fugacity is greatly different, the change of oxygen fugacity has little effect on the valence state of tungsten, while uranium is a highly sensitive element in redox (Wang et al., 2020; Zhu et al., 2020; Zhang et al., 2017). Consequently, the W concentrations in the ore-forming fluids will increase with the evolution due to the change of possible redox conditions, resulting in the discordance of W-U pairs (Fig. 11d). Specifically, Heinrich (1990) proposed that the precipitation of tin in hydrothermal fluids is:



This indicates that the relatively acidic environment with more hydrogen is not conducive to the precipitation of cassiterite, and the reaction above may be reversed, that is, there is a trend of decreasing oxygen fugacity with evolution. Similarly, this conclusion is also supported by Ji et al. (2021a), which showed the  $\lg f_{\text{O}_2}$  varied from -16 to -17.5 as the magma temperature decreased.

Indium is moderately to highly incompatible during mantle melting, and tends to concentrate in highly fractionated magma (Sun, 1982). Accordingly, Indium concentrations are particularly high in some granite-related Sn-polymetallic vein systems, and the principal In hosts are sphalerite, chalcopyrite and stannite group minerals with local concentrations within cassiterite and tennantite (e.g., Ishihara et al., 2006; Cook et al., 2009; Pavlova et al., 2015; Andersen et al., 2016). Generally, the In contents in cassiterite from cassiterite-quartz veins or Sn-sulfide veins are less than 1000 ppm (Pavlova et al., 2015; Andersen et al., 2016). It is noteworthy that the abnormally high concentrations of In (2004–2702 ppm, average of 2335 ppm) in cassiterite in the Maodeng deposit, which is much higher than most other Sn-polymetallic deposits worldwide (e.g., Gejiu: 25–50 ppm, Far East: 40–485 ppm, Bolivian: 32–801 ppm) (Li et al., 2007; Pavlova et al., 2015; Andersen et al., 2016; Xu and Li, 2018; Gemmrich et al., 2021), although it may be an interference due to high Sn contents here. Considering the indium of chalcophile character, Ishihara et al. (2006) proposed that the magnetite-series magmatism is also important for In-concentration, because of

availability of sulfur (e.g., Hattori and Keith, 2001). He further suggested that the two magmatic activities differing (i.e., granitic magma, deeply generated oxidized magma) in oxygen and sulfur fugacities together responsible for the high concentration of indium in ore deposits of the Japanese Island arcs. Similarly, Pavlova et al. (2015) also argued that the combined contribution from granite and mafic magmatism produced fluids leads to the formation of high grade indium in both cassiterites and sulfides from the ore deposits in Russia. Thus, injection of mantle melt/fluid may be one of the main reasons why indium is rich in Maodeng deposit, as discussed in Section 7.2.3. Meanwhile, the high concentration of indium in ores indicate that intense fluid-rock reaction may be occurred during the ore mineralization process, because the low In contents (<0.12 wt%; Ji et al., 2021a) in Maodeng granites but indium-rich in sedimentary source rocks (e.g., Ishihara et al., 2006).

To sum up, the chemical features of cassiterites in the different mineralization stages indicate the changes in physicochemical condition of ore-forming fluids. The ore-forming process experienced fluid cooling and the volatile content (especially fluorine) increasing. The abnormal high indium concentrations may be caused by the addition of mantle-derived fluids or the strong fluid-rock reaction.

## 8. Conclusions

On the basis of new geochemical data of zircon and cassiterite, and U-Pb dating of the granite porphyry and cassiterite from the Maodeng Sn-Cu deposit, the conclusions are as follows:

- (1) Zircon LA-ICP-MS U-Pb age of granite porphyry is  $134.6 \pm 0.4$  Ma, and the LA-ICP-MS U-Pb ages of cassiterites from early and late stage are  $140 \pm 7$  Ma and  $137 \pm 6$  Ma, respectively, suggesting an Early Cretaceous Sn-Cu mineralization under the Paleo-Pacific plate slab roll-back setting.
- (2) The ore-related granite porphyry (complementary phase) is more differentiated and reduced than the porphyry monzogranite (main phase). Furthermore, the granites associated with Cu-rich Sn deposits are characterized by higher oxygen fugacity, lower differential degree and aluminum saturation index (ASI) than those of Sn-W deposits, which address the limited scale of Sn mineralization in Sn-Cu deposits.
- (3) Trace elements variations in cassiterites from different stages suggest that the ore-forming process experienced the cooling, increasing volatile contents and fluid-rock reaction.
- (4) The Maodeng Sn-Cu deposit may result from the oxidized Cu-rich fluids exsolved from the upwelling mantle magma inject to the reduced, Sn-rich magma chambers. The Cu and Sn metals come from the mantle magma and crustal granitic magma, respectively, and that Sn-Cu mineralization are more likely a product of spatial coupling.

## Declaration of Competing Interest

The authors declare that they have no known competing financial interests or personal relationships that could have appeared to influence the work reported in this paper.

## Data availability

Data will be made available on request.

## Acknowledgments

This research was financially supported by the National Key R&D Program of China (Grant No. 2019YFC0605202), the CAGS Research Fund (Grant No. KK2208), and the National Natural Science Foundation of China (Grant No. 41772084). Prof. Kejun Hou and Dr. Qian Wang are thanked for providing assistance during in situ U-Pb dating and trace

element analyses of minerals.

## Appendix A. Supplementary data

Supplementary data to this article can be found online at <https://doi.org/10.1016/j.oregeorev.2022.105159>.

## References

- Andersen, J.C., Stickland, R.J., Rollinson, G.K., Shail, R.K., 2016. Indium mineralisation in SW England: host parageneses and mineralogical relations. *Ore Geol. Rev.* 78, 213–238.
- Ballard, J.R., Palin, M.J., Campbell, I.H., 2002. Relative oxidation states of magmas inferred from Ce (IV)/Ce (III) in zircon: application to porphyry copper deposits of northern Chile. *Contrib. Mineral. Petrol.* 144, 347–364.
- Ballouard, C., Poujol, M., Boulvais, P., Branquet, Y., Tartese, R., Vigneresse, J.L., 2016. Nb-Ta fractionation in peraluminous granites: A marker of the magmatic-hydrothermal transition. *Geology* 44, 231–234.
- Ballouard, C., Massyeau, M., Elburg, M.A., Tappe, S., Viljoen, F., Brandenburg, J.T., 2020. The magmatic and magmatic-hydrothermal evolution of felsic igneous rocks as seen through Nb-Ta geochemical fractionation, with implications for the origins of rare-metal mineralizations. *Earth-Sci. Rev.* 203, 103115.
- Blevin, P.L., 2004. Redox and compositional parameters for interpreting the granitoid metallogeny of eastern Australia: Implications for gold-rich ore systems. *Resour. Geol.* 54, 241–252.
- Blevin, P.L., Chappell, B.W., Allen, C.M., 1996. Intrusive metallogenetic provinces in eastern Australia based on granite source and composition. *Trans. R. Soc. Edinb. Earth Sci.* 87, 281–290.
- Cerný, P., Blevin, P.L., Cuney, M., London, D., 2005. Granite-related ore deposits. *Soc. Econ. Geol.* 100, 337–370.
- Cheng, Y., Spandler, C., Kemp, A., Mao, J., Rusk, B., Hu, Y., Blake, K., 2019. Controls on cassiterite ( $\text{SnO}_2$ ) crystallization: Evidence from cathodoluminescence, trace-element chemistry, and geochronology at the Gejiu Tin District. *Am. Mineral.* 104, 118–129.
- Cheng, T.S., Yang, W.J., Wang, D.H., 2014. Zircon U-Pb age and geochemical characteristics of the Alubaoge A-type granite in Xiwuqi, Inner Mongolia and its geological significance. *Geotecton. Metallog.* 38, 718–728 in Chinese with English abstract.
- Cook, N.J., Ciobanu, C.L., Pring, A., Skinner, W., Shimizu, M., Danyushevsky, L., Saini-Eidukat, B., Melcher, F., 2009. Trace and minor elements in sphalerite: A LA-ICPMS study. *Geochim. Cosmochim. Acta* 73, 4761–4791.
- Deering, C.D., Keller, B., Schoene, B., Bachmann, O., Beane, R., Ovtcharova, M., 2016. Zircon record of the plutonic-volcanic connection and protracted rhyolite melt evolution. *Geology* 44, 267–270.
- Duc-Tin, Q., Audétat, A., Keppler, H., 2007. Solubility of tin in (Cl, F)-bearing aqueous fluids at  $700^\circ\text{C}$ , 140 MPa: A LA-ICP-MS study on synthetic fluid inclusions. *Geochim. Cosmochim. Acta* 71, 3323–3335.
- Eggins, S.M., Shelley, J.M.G., 2002. Compositional heterogeneity in NIST SRM 610–617 glasses. *Geostand. Newsl.* 26, 269–286.
- Gao, X., Zhou, Z., Breiter, K., Ouyang, H., Liu, J., 2019. Ore-formation mechanism of the Weilasius tin-polymetallic deposit, NE China: constraints from bulk-rock and mica chemistry, He-Ar isotopes, and Re-Os dating. *Ore Geol. Rev.* 109, 163–183.
- Gardiner, N.J., Hawkesworth, C.J., Robb, L.J., Whitehouse, M.J., Roberts, N.M., Kirkland, C.L., Evans, N.J., 2017. Contrasting granite metallogeny through the zircon record: a case study from Myanmar. *Sci. Rep.* 7, 1–9.
- Ge, W.C., Lin, Q., Sun, D.Y., Wu, F.Y., Won, C.K., Lee, M.W., Jin, M.S., Yun, S.H., 1999. Geochemical characteristics of the Mesozoic basalts in Da Hinggan Ling: evidence of the mantle-crust interaction. *Acta Petrol. Sin.* 15, 396–407 in Chinese with English abstract.
- Gemmrich, L., Torró, L., Melgarejo, J.C., Laurent, O., Vallance, J., Chelle-Michou, C., Sempere, T., 2021. Trace element composition and U-Pb ages of cassiterite from the Bolivian tin belt. *Miner. Depos.* 56, 1491–1520.
- Günther, D., Jackson, S.E., Longerich, H.P., 1999. Laser ablation and arc/spark solid sample introduction into inductively coupled plasma mass spectrometers. *Spectrochim. Acta Part B* 54, 381–409.
- Guo, S., He, P., Zhang, X.B., Cui, Y.R., Zhang, T.F., Zhang, K., Lai, L., Liu, C.B., 2019. Geochronology and geochemistry of Maodeng-Xiaogushan tin-polymetallic ore-field in southern Da Hinggan Mountains and their geological significances. *Min. Depos.* 38, 509–525 in Chinese with English abstract.
- Guo, J., Zhang, R., Sun, W., Ling, M., Hu, Y., Wu, K., Zhang, L., 2018a. Genesis of tin-dominant polymetallic deposits in the Dachang district, South China: Insights from cassiterite U-Pb ages and trace element compositions. *Ore Geol. Rev.* 95, 863–879.
- Guo, J., Zhang, R., Li, C., Sun, W., Hu, Y., Kang, D., Wu, J., 2018b. Genesis of the Gaosong Sn-Cu deposit, Gejiu district, SW China: Constraints from in situ LA-ICP-MS cassiterite U-Pb dating and trace element fingerprinting. *Ore Geol. Rev.* 92, 627–642.
- Harlaux, M., Kouzmanov, K., Gialli, S., Laurent, O., Rielli, A., Dini, A., Chauvet, A., Menzies, A., Kalinaj, M., Fontboté, L., 2020. Tourmaline as a tracer of late-magmatic hydrothermal fluid evolution: the world-class San Rafael tin (-copper) deposit, Peru. *Econ. Geol.* 115, 1665–1697.
- Harlaux, M., Kouzmanov, K., Gialli, S., Marger, K., Bouvier, A.S., Baumgartner, L.P., Rielli, A., Dini, A., Chauvet, A., Kalinaj, M., Fontboté, L., 2021a. Fluid mixing as primary trigger for cassiterite deposition: Evidence from in situ  $\delta^{18}\text{O}$ - $\delta^{11}\text{B}$  analysis of

- tourmaline from the world-class San Rafael tin (-copper) deposit, Peru. *Earth Planet. Sci. Lett.* 563, 116889.
- Harlaux, M., Kouzmanov, K., Gialli, S., Clark, A.H., Laurent, O., Corthay, G., Flores, E.P., Dini, A., Chauvet, A., Ulianov, A., Chiaradia, M., Menzies, A., Durand, G.V., Kalinaj, M., Fontboté, L., 2021b. The upper Oligocene San Rafael intrusive complex (Eastern Cordillera, southeast Peru), host of the largest-known high-grade tin deposit. *Lithos* 400, 106409.
- Hattori, K.H., Keith, J.D., 2001. Contribution of mafic melt to porphyry copper mineralization: evidence from Mount Pinatubo, Philippines, and Bingham Canyon, Utah, USA. *Miner. Depos.* 36, 799–806.
- Heinrich, C.A., 1990. The chemistry of hydrothermal tin (-tungsten) ore deposition. *Econ. Geol.* 85, 457–481.
- Hoskin, P.W., Schaltegger, U., 2003. The composition of zircon and igneous and metamorphic petrogenesis. *Rev. Mineral. Geochem.* 53, 27–62.
- Ishihara, S., 1981. The granitoid series and mineralization. *Econ. Geol.* 75th Anniv. Vol. 458–484.
- Ishihara, S., Hoshino, K., Murakami, H., Endo, Y., 2006. Resource evaluation and some genetic aspects of indium in the Japanese ore deposits. *Resour. Geol.* 56, 347–364.
- Jackson, S.E., Pearson, N.J., Griffin, W.L., Belousov, E.A., 2004. The application of laser ablation-inductively coupled plasma-mass spectrometry to in situ U-Pb zircon geochronology. *Chem. Geol.* 211, 47–69.
- Ji, G.Y., Jiang, S.H., Zhang, L.S., Li, G.F., Liu, Y.F., Yi, J.J., Zhang, S.J., 2021a. Petrogenic and metallogenetic significance of Alubaogeshan granite in Maodeng deposit of southern Da Hinggan Mountains: Evidence from mineralogy of zircon, amphibole and biotite. *Min. Depos.* 40, 449–474 in Chinese with English abstract.
- Ji, G.Y., Jiang, S.H., Li, G.F., Yi, J.J., Zhang, L.L., Liu, Y.F., 2021b. Metallogenetic control of magmatism on the Maodeng Sn-Cu deposit in the southern Great Xing'an Range: Evidence from geochronology, geochemistry, and Sr-Nd-Pb isotopes. *Geotecton. Metallog.* 45, 681–704 in Chinese with English abstract.
- Ji, G., Jiang, S., Zhang, L., Liu, Y., Zhang, L., 2022. Chronology and geochemical characteristics of the highly fractionated alkali feldspar granite from the Maodeng deposit in the southern Great Xing'an Range. *Acta Petrol. Sin.* 38, 855–882 in Chinese with English abstract.
- Jiang, S.H., Bagas, L., Hu, P., Han, N., Chen, C.L., Liu, Y., Kang, H., 2016. Zircon U-Pb ages and Sr-Nd-Hf isotopes of the highly fractionated granite with tetrad REE patterns in the Shamai tungsten deposit in eastern Inner Mongolia, China: implications for the timing of mineralization and ore genesis. *Lithos* 261, 322–339.
- Jiang, S.Y., Wen, H.J., Xu, C., Wang, Y., Su, H.M., Sun, W.D., 2019. Earth sphere cycling and enrichment mechanism of critical metals: Major scientific issues for future research. *Bull. Natl. Nat. Sci. Found. China* 33, 112–118 in Chinese with English abstract.
- Jugo, P.J., Luth, R.W., Richards, J.P., 2005. Experimental data on the speciation of sulfur as a function of oxygen fugacity in basaltic melts. *Geochim. Cosmochim. Acta* 69, 497–503.
- Jugo, P.J., Wilke, M., Botcharnikov, R.E., 2010. Sulfur K-edge XANES analysis of natural and synthetic basaltic glasses: Implications for S speciation and S content as function of oxygen fugacity. *Geochim. Cosmochim. Acta* 74, 5926–5938.
- Lehmann, B., 1990. Metallogeny of Tin. Springer, Berlin, p. 211.
- Lehmann, B., 2021. Formation of tin ore deposits: A reassessment. *Lithos* 402, 105756.
- Lehmann, B., Ishihara, S., Michel, H., Miller, J., Rapela, C.W., Sanchez, A., Tistl, M., Winkelmann, L., 1990. The Bolivian tin province and regional tin distribution in the Central Andes: a reassessment. *Econ. Geol.* 85, 1044–1058.
- Li, Y., Brouwer, F.M., Xiao, W., Zheng, J., 2017b. A Paleozoic fore-arc complex in the eastern Central Asian Orogenic Belt: Petrology, geochemistry and zircon U-Pb-Hf isotopic composition of paragneisses from the Xilingol Complex in Inner Mongolia, China. *Gondwana Res.* 47, 323–341.
- Li, S., Chung, S.L., Wang, T., Wilde, S.A., Chu, M.F., Guo, Q.Q., 2017a. Tectonic significance and geodynamic processes of large-scale Early Cretaceous granitoid magmatic events in the southern Great Xing'an Range, North China. *Tectonics* 36, 615–633.
- Li, S., Chung, S.L., Wang, T., Wilde, S.A., Chu, M.F., Pang, C.J., Guo, Q.Q., 2018. Water-fluxed crustal melting and petrogenesis of large-scale Early Cretaceous intracontinental granitoids in the southern Great Xing'an Range, North China. *Geol. Soc. Am. Bull.* 130, 580–597.
- Li, X., Watanabe, Y., Mao, J., 2007. Research situation and economic value of indium deposits. *Mineral Deposits* 26, 475 in Chinese with English abstract.
- Li, J., Huang, X.L., Fu, Q., Li, W.X., 2021a. Tungsten mineralization during the evolution of a magmatic-hydrothermal system: Mineralogical evidence from the Xihuashan rare-metal granite in South China. *Am. Mineral.* 106, 443–460.
- Li, Q., Zhao, K.D., Palmer, M.R., Chen, W., Jiang, S.Y., 2021b. Exploring volcanic-intrusive connections and chemical differentiation of high silica magmas in the Early Cretaceous Yanbel caldera complex hosting a giant tin deposit. Southeast China. *Chem. Geol.* 584, 120501.
- Liao, Z., Wang, Y.W., Wang, J.B., Li, H.M., Long, L.L., 2014. Cassiterite LA-MC-ICP-MS U-Pb dating of Dajing tin polymetallic deposit in Inner Mongolia and its significance. *Min. Depos.* Z1, 421–422 in Chinese with English abstract.
- Liu, Y., 1996a. Geology and origin of the Maodeng tin-copper deposit, Inner Mongolia. *Min. Depos.* 15, 143–154.
- Liu, Y., 1996b. Metallogenic zoning and origin of the Maodeng tin-copper deposit. *Min. Depos.* 15, 329–338.
- Liu, Y., Gao, S., Hu, Z., Gao, C., Zong, K., Wang, D., 2010. Continental and oceanic crust recycling-induced melt-peridotite interactions in the Trans-North China Orogen: U-Pb dating, Hf isotopes and trace elements in zircons from mantle xenoliths. *J. Petrol.* 51, 537–571.
- Liu, X., Li, X.G., Zhu, X.Y., Sun, Y.L., Jiang, H.Y., Jiang, B.B., Wang, H., Cheng, X.Y., 2017. Mineralization process of the Baiyinchagan tin polymetallic deposit in Inner Mongolia II: Chronology of ore-bearing porphyry, geochemical characteristics and geological implications of the granite porphyry. *Miner. Explor.* 8, 981–996 in Chinese with English abstract.
- Liu, C.B., Wang, Q., Wang, J.Z., Lang, X.X., Zhang, M., Hou, G.Y., 2018. Significance of geological features and U-Pb chronology features, Alubaogeshan granite-porphyry, MaoDeng area of Inner Mongolia. *Miner. Explor.* 1316–1321 in Chinese with English abstract.
- Ludwig, K.R., 2003. Isoplot 3.00: A geochronological toolkit for Microsoft Excel. Berkeley Geochronology Center Special Publication 4, 70.
- Mao, J.W., Cheng, Y.B., Chen, M.H., Pirajno, F., 2013. Major types and time-space distribution of Mesozoic ore deposits in South China and their geodynamic settings. *Min. Depos.* 48, 267–294.
- Mao, J.W., Yuan, S.D., Xie, G.Q., Song, S.W., Zhou, Q., Gao, Y.B., Liu, X., Fu, X.F., Cao, J., Zeng, Z.L., Li, T.G., Fan, X.Y., 2019a. New advances on metallogenetic studies and exploration on critical minerals of China in 21st century. *Min. Depos.* 38, 935–969 in Chinese with English abstract.
- Mao, J.W., Ouyang, H.G., Song, S.W., Santosh, M., Yuan, S.D., Zhou, Z.H., Zheng, W., Liu, H., Liu, P., Cheng, Y.B., Chen, M.H., 2019b. Geology and metallogeny of tungsten and tin deposits in China. *Econ. Geol. (Spec. Publ.)* 22, 411–482.
- Mao, W., Zhong, H., Yang, J., Tang, Y., Liu, L., Fu, Y., Zhang, X., Sein, K., Aung, S., Zhang, L., 2020. Combined zircon, molybdenite, and cassiterite geochronology and cassiterite geochemistry of the Kuntabin tin-tungsten deposit in Myanmar. *Econ. Geol.* 115, 603–625.
- Möller, P., Dulski, P., Szacki, W., Malow, G., Riedel, E., 1988. Substitution of tin in cassiterite by tantalum, niobium, tungsten, iron and manganese. *Geochim. Cosmochim. Acta* 52, 1497–1503.
- Nasdala, L., Corfu, F., Valley, J.W., Spicuzza, M.J., Wu, F.Y., Li, Q.L., Yang, Y.H., Fisher, C., Münker, C., Kennedy, A.K., Reiners, P.W., Kronz, A., Wiedenbeck, M., Wirth, R., Chanmuang, C., Zeug, M., Václav, T., Norberg, N., Häger, T., Kröner, A., Hofmeister, W., 2016. Zircon MI27–A homogeneous reference material for SIMS U-Pb geochronology combined with hafnium, oxygen and potentially, lithium isotope analysis. *Geostand. Geanal. Res.* 40, 457–475.
- Nie, F.J., Jiang, S.H., Zhang, Y., Bai, D.M., Hu, P., Zhao, Y.Y., Liu, Y., 2007. Metallogenetic studies and prospecting orientation in central and eastern segments along China-Mongolia border. Geological Publishing House, 1–574.
- Niu, X., Shu, Q., Xing, K., Yuan, S., Wei, L., Zhang, Y., Yu, F., Zeng, Q., Ma, S., 2022. Evaluating Sn mineralization potential at the Haobugao skarn Zn-Pb deposit (NE China) using whole-rock and zircon geochemistry. *J. Geochem. Explor.* 234, 106938.
- Ouyang, H.G., Mao, J.W., Santosh, M., Zhou, J., Zhou, Z.H., Wu, Y., Hou, L., 2013. Geodynamic setting of Mesozoic magmatism in NE China and surrounding regions: perspectives from spatio-temporal distribution patterns of ore deposits. *J. Asian Earth Sci.* 78, 222–236.
- Ouyang, H., Mao, J., Zhou, Z., Su, H., 2015. Late Mesozoic metallogeny and intracontinental magmatism, southern Great Xing'an Range, northeastern China. *Gondwana Res.* 27, 1153–1172.
- Ouyang, H.G., Wu, X.L., Mao, J.W., Santosh, M., Zhou, Z.H., Li, C., Su, H.M., 2014. The nature and timing of ore formation in the Budunhua copper deposit, southern Great Xing'an Range: evidence from geology, fluid inclusions, and U-Pb and Re-Os geochronology. *Ore Geol. Rev.* 63, 238–251.
- Pavlova, G.G., Palessky, S.V., Borisenko, A.S., Vladimirov, A.G., Seifert, T., Phan, L.A., 2015. Indium in cassiterite and ores of tin deposits. *Ore Geol. Rev.* 66, 99–113.
- Richards, J.P., 2011. High Sr/Y arc magmas and porphyry Cu±Mo±Au deposits: just add water. *Econ. Geol.* 106, 1075–1081.
- Richards, J.P., 2015. The oxidation state, and sulfur and Cu contents of arc magmas: implications for metallogeny. *Lithos* 233, 27–45.
- Romer, R.L., Kröner, U., 2016. Phanerozoic tin and tungsten mineralization-tectonic controls on the distribution of enriched protoliths and heat sources for crustal melting. *Gondwana Res.* 31, 60–95.
- Sato, K., 2012. Sedimentary Crust and Metallogeny of Granitoid Affinity: Implications from the Geotectonic Histories of the Circum-Japan Sea Region, Central Andes and Southeastern Australasia. *Resour. Geol.* 62, 329–351.
- Sengör, A.M.C., Natal'In, B.A., Burtman, V.S., 1993. Evolution of the Altaiid tectonic collage and Palaeozoic crustal growth in Eurasia. *Nature* 364, 299–307.
- Shannon, R.T., Prewitt, C.T., 1969. Effective ionic radii in oxides and fluorides. *Acta Crystallogr. Sect. B Struct. Crystallogr. Cryst. Chem.* 25, 925–946.
- Shannon, R.T., Prewitt, C.T., 1970. Revised values of effective ionic radii. *Acta Crystallogr. Sect. B Struct. Crystallogr. Cryst. Chem.* 26, 1046–1048.
- Shao, J.A., Zhang, L.Q., Xiao, Q.H., Li, X.B., 2005. Rising of Da Hinggan Mts in Mesozoic: A possible mechanism of intracontinental orogeny. *Acta Petrol. Sin.* 21, 789–794 in Chinese with English abstract.
- Shao, J.A., Mu, B.L., Zhu, H.Z., Zhang, L.Q., 2010. Material source and tectonic settings of the Mesozoic mineralization or the Da Hinggan Mts. *Acta Petrol. Sin.* 26, 649–656 in Chinese with English abstract.
- Shi, G., Liu, D., Zhang, F., Jian, P., Miao, L., Shi, Y., Tao, H., 2003. SHRIMP U-Pb zircon geochronology and its implications on the Xilin Gol Complex, Inner Mongolia, China. *Chin. Sci. Bull.* 48, 2742–2748.
- Shu, Q.H., Lai, Y., Sun, Y., Wang, C., Meng, S., 2013. Ore genesis and hydrothermal evolution of the Baiyinuo'er zinc-lead skarn deposit, Northeast China: evidence from isotopes (S, Pb) and fluid inclusions. *Econ. Geol.* 108, 835–860.
- Shu, Q.H., Chang, Z.S., Lai, Y., Hu, X., Wu, H., Zhang, Y., Wang, P., Zhai, D.G., Zhang, C., 2019. Zircon trace elements and magma fertility: insights from porphyry (-skarn) Mo deposits in NE China. *Min. Depos.* 54, 645–656.
- Shu, Q.H., Chang, Z.S., Mavrogenes, J., 2021. Fluid compositions reveal fluid nature, metal deposition mechanisms, and mineralization potential: An example at the Haobugao Zn-Pb skarn, China. *Geology* 49, 473–477.
- Sillitoe, R.H., Lehmann, B., 2022. Copper-rich tin deposits. *Min. Depos.* 57, 1–11.

- Sillitoe, R.H., Halls, C., Grant, J.N., 1975. Porphyry tin deposits in Bolivia. *Econ. Geol.* 70, 913–927.
- Sláma, J., Košler, J., Condon, D.J., Crowley, J.L., Gerdes, A., Hanchar, J.M., Horstwood, M.S.A., Morris, G.A., Nasdala, L., Norberg, N., Schaltegger, U., Schoene, B., Tubrett, M.M., Whitehouse, M.J., 2008. Plešovice zircon—a new natural reference material for U-Pb and Hf isotopic microanalysis. *Chem. Geol.* 249, 1–35.
- Sun, S.S., 1982. Chemical composition and origin of the Earth's primitive mantle. *Geochim. Cosmochim. Acta* 46, 179–192.
- Sun, W., Huang, R.F., Li, H., Hu, Y.B., Zhang, C.C., Sun, S.J., Zhang, L.P., Ding, X., Li, C.Y., Zartman, R.E., Ling, M.X., 2015. Porphyry deposits and oxidized magmas. *Ore Geol. Rev.* 65, 97–131.
- Sun, W.D., Liang, H.Y., Ling, M.X., Zhan, M.Z., Ding, X., Zhang, H., Yang, X.Y., Li, Y.L., Ireland, T.R., Wei, Q.R., Fan, W.M., 2013. The link between reduced porphyry copper deposits and oxidized magmas. *Geochim. Cosmochim. Acta* 103, 263–275.
- Sun, S.S., McDonough, W.F., 1989. Chemical and isotopic systematics of oceanic basalts: implications for mantle composition and processes. Geological Society, London Special Publications 42, 313–345.
- Taylor, R., 1979. *Geology of Tin Deposits*. Elsevier, New York, p. 543 p..
- Taylor, J.R., Wall, V.J., 1993. Cassiterite solubility, tin speciation, and transport in a magmatic aqueous phase. *Econ. Geol.* 88, 437–460.
- Tindle, A.G., Breaks, F.W., 1998. Oxide minerals of the Separation Rapids rare-element granitic pegmatite group, northwestern Ontario. *Can. Mineral.* 36, 609–635.
- Trail, D., Watson, E.B., Tailby, N.D., 2011. The oxidation state of Hadean magmas and implications for early Earth's atmosphere. *Nature* 480, 79–82.
- Trail, D., Watson, E.B., Tailby, N.D., 2012. Ce and Eu anomalies in zircon as proxies for the oxidation state of magmas. *Geochim. Cosmochim. Acta* 97, 70–87.
- Wang, F., Bagas, L., Jiang, S., Liu, Y., 2017. Geological, geochemical, and geochronological characteristics of Weilasitu Sn-polymetallic deposit, Inner Mongolia, China. *Ore Geol. Rev.* 80, 1206–1229.
- Wang, Z.Q., Chen, B., Ma, X.H., 2014. In situ LA-ICP-MS U-Pb age and geochemical data of cassiterite of the Furong tin deposit, the Nanling Range: Implications for the origin and evolution of the ore-forming fluid. *Chin. Sci. Bull.* 59, 2505–2519 in Chinese with English abstract.
- Wang, K., Deng, J., Hao, X., 2020. The geochemical behavior of uranium and mineralization: South China uranium province as an example. *Acta Petrol. Sin.* 36, 35–43.
- Wang, Y.W., Shi, Y.X., Wang, Y.S., 1996. Geological and geochemical characteristics of ore-forming volcanic intrusive complex in Maodeng Sn-Cu deposit. *Geology of Inner Mongolia (Z1)*: 26–35 in Chinese with English abstract.
- Wang, J.B., Wang, Y.W., Wang, L.J., Uemoto, T., 2001. Tin-polymetallic mineralization in the southern part of the Da Hinggan Mountains. *China. Resour. Geol.* 51, 283–291.
- Wang, J.B., Wang, Y.W., Wang, L.J., 2005. Tin-polymetallic metallogenetic series in the southern part of Da Hinggan Mountains, China. *Geol. Prospect.* 41, 15–20 in Chinese with English abstract.
- Wang, J., Williams-Jones, A.E., Timofeev, A., Liu, J., Yuan, S., 2022. An experimental investigation of the solubility and speciation of scandium in fluoride-bearing aqueous liquids at temperatures up to 250 °C. *Geochim. Cosmochim. Acta*. <https://doi.org/10.1016/j.gca.2022.01.032>.
- Wang, T., Zheng, Y., Zhang, J., Zeng, L., Donskaya, T., Guo, L., Li, J., 2011. Pattern and kinematic polarity of late Mesozoic extension in continental NE Asia: Perspectives from metamorphic core complexes. *Tectonics* 30, TC6007.
- Wang, T., Guo, L., Zhang, L., Yang, Q., Zhang, J., Tong, Y., Ye, K., 2015. Timing and evolution of Jurassic-Cretaceous granitoid magmatism in the Mongol-Okhotsk belt and adjacent areas, NE Asia: Implications for transition from contractional crustal thickening to extensional thinning and geodynamic settings. *J. Asian Earth Sci.* 97, 365–392.
- Wang, B., Niu, S., Sun, A., Hu, H., Liu, Y., Guo, L., Wang, S., 2008. Helium-argon isotopic tracing for the Pb-Zn-Ag polymetallic ore deposits in the central-south segment of the Da Hinggan Ling Range. *Chin. J. Geochem.* 27, 235–241.
- Wilde, S.A., 2015. Final amalgamation of the Central Asian Orogenic Belt in NE China: Paleo-Asian Ocean closure versus Paleo-Pacific plate subduction—A review of the evidence. *Tectonophysics* 662, 345–362.
- Wilde, S.A., Zhou, J.B., 2015. The late Paleozoic to Mesozoic evolution of the eastern margin of the Central Asian Orogenic Belt in China. *J. Asian Earth Sci.* 113, 909–921.
- Wolf, M., Romer, R.L., Franz, L., López-Moro, F.J., 2018. Tin in granitic melts: The role of melting temperature and protolith composition. *Lithos* 310, 20–30.
- Wu, J., Kong, H., Li, H., Algeo, T.J., Yonezu, K., Liu, B., Wu, Q.H., Zhu, D.P., Jiang, H., 2021. Multiple metal sources of coupled Cu-Sn deposits: Insights from the Tongshanling polymetallic deposit in the Nanling Range, South China. *Ore Geol. Rev.* 139, 104521.
- Wu, F., Liu, X., Ji, W., Wang, J., Yang, L., 2017. Highly fractionated granites: Recognition and research. *Sci. China Earth Sci.* 60, 1201–1219 in Chinese with English abstract.
- Wu, F.Y., Sun, D.Y., Ge, W.C., Zhang, Y.B., Grant, M.L., Wilde, S.A., Jahn, B.M., 2011. Geochronology of the Phanerozoic granitoids in northeastern China. *J. Asian Earth Sci.* 41, 1–30.
- Wu, F.Y., Liu, X.C., Liu, Z.C., Wang, R.C., Xie, L., Wang, J.M., Ji, W.Q., Yang, L., Liu, C., Khanal, G., He, S.X., 2020. Highly fractionated Himalayan leucogranites and associated rare-metal mineralization. *Lithos* 352, 105319.
- Xiao, W.J., Windley, B.F., Huang, B.C., Han, C.M., Yuan, C., Chen, H.L., Sun, M., Sun, S., Li, J.L., 2009. End-Permian to mid-Triassic termination of the accretionary processes of the southern Altai: implications for the geodynamic evolution, Phanerozoic continental growth, and metallogeny of Central Asia. *Int. J. Earth Sci.* 98, 1189–1217.
- Xu, J., Li, X.F., 2018. Spatial and temporal distributions, metallogenetic backgrounds and processes of indium deposits. *Acta Petrologica Sinica* 34, 3611–3626 in Chinese with English abstract.
- Xu, W.L., Pei, F.P., Wang, F., Meng, E., Ji, W.Q., Yang, D.B., Wang, W., 2013. Spatial-temporal relationships of Mesozoic volcanic rocks in NE China: constraints on tectonic overprinting and transformations between multiple tectonic regimes. *J. Asian Earth Sci.* 74, 167–193.
- Xu, W.L., Sun, C.Y., Tang, J., Luan, J.P., Wang, F., 2019. Basement nature and tectonic evolution of the Xing'an-Mongolian Orogenic Belt. *Earth Sci.* 44 1620–1646 in Chinese with English abstract.
- Yang, Z.M., Hou, Z.Q., Song, Y.C., Li, Z.Q., Xia, D.X., Pan, F.C., 2008. Qulong superlarge porphyry Cu deposit in Tibet: Geology, alteration and mineralization. *Min. Depos.* 27, 279–318 in Chinese with English abstract.
- Yang, F., Sun, J., Wang, Y., Fu, J., Na, F., Fan, Z., Hu, Z., 2019. Geology, geochronology and geochemistry of Weilasitu Sn-polymetallic deposit in Inner Mongolia, China. *Minerals* 9, 104.
- Yao, L., Lü, Z.C., Ye, T.Z., Pang, Z.S., Jia, H.X., Zhang, Z.H., Wu, Y.F., Li, R.H., 2017. Zircon U-Pb age, geochemical and Nd-Hf isotopic characteristics of quartz porphyry in the Baiyinchagan Sn polymetallic deposit, Inner Mongolia, southern Great Xing'an Range, China. *Acta Petrol. Sin.* 33, 3183–3199 in Chinese with English abstract.
- Yuan, S., Peng, J., Hao, S., Li, H., Geng, J., Zhang, D., 2011. In situ LA-ICP-MS and ID-TIMS U-Pb geochronology of cassiterite in the giant Furong tin deposit, Hunan Province, South China: New constraints on the timing of tin-polymetallic mineralization. *Ore Geol. Rev.* 43, 235–242.
- Yuan, S.D., Williams-Jones, A.E., Romer, R.L., Zhao, P., Mao, J., 2019. Protolith-related thermal controls on the decoupling of Sn and W in Sn-W metallogenetic provinces: Insights from the Nanling region, China. *Econ. Geol.* 114, 1005–1012.
- Yuan, S.D., Zhao, P.L., Liu, M., 2020. Some problems involving in petrogenesis and metallogenesis of granite-related tin deposits. *Min. Depos.* 39, 607–618 in Chinese with English abstract.
- Zajacz, Z., Candela, P.A., Piccoli, P.M., Sanchez-Valle, C., Wälde, M., 2013. Solubility and partitioning behavior of Au, Cu, Ag and reduced S in magmas. *Geochim. Cosmochim. Acta* 112, 288–304.
- Zhai, D., Williams-Jones, A.E., Liu, J., Selby, D., Voudouris, P.C., Tombros, S., Li, K., Li, P.L., Sun, H., 2020. The Genesis of the Giant Shuangjianzishan Epithermal Ag-Pb-Zn Deposit, Inner Mongolia, Northeastern China. *Econ. Geol.* 115, 101–128.
- Zhang, R., Lu, J., Lehmann, B., Li, C., Li, G., Zhang, L., Guo, J., Sun, W., 2017. Combined zircon and cassiterite U-Pb dating of the Piaotang granite-related tungsten-tin deposit, southern Jiangxi tungsten district, China. *Ore Geol. Rev.* 82, 268–284.
- Zhang, Q.M., Zhai, D.X., Li, H., 2013. Geological characteristics and deposit genesis of Maodeng molybdenum-tin-copper deposit, Inner Mongolia. *Miner. Explor.* 4, 248–256 in Chinese with English abstract.
- Zhao, Y., Chen, S., Tian, H., Zhao, J., Tong, X., Chen, X., 2021. Trace element and S isotope characterization of sulfides from skarn Cu ore in the Laochang Sn-Cu deposit, Gejiu district, Yunnan, China: Implications for the ore-forming process. *Ore Geol. Rev.* 134, 104155.
- Zhao, P., Zajacz, Z., Tsay, A., Yuan, S., 2022a. Magmatic-hydrothermal tin deposits form in response to efficient tin extraction upon magma degassing. *Geochim. Cosmochim. Acta* 316, 331–346.
- Zhao, P., Yuan, S., Williams-Jones, A.E., Romer, R.L., Yan, C., Song, S., Mao, J., 2022b. Temporal Separation of W and Sn Mineralization by Temperature-Controlled Incongruent Melting of a Single Protolith: Evidence from the Wangxianling Area, Nanling Region, South China. *Econ. Geol.* 117, 667–682.
- Zhao, P., Chu, X., Williams-Jones, A.E., Mao, J., Yuan, S., 2022c. The role of phyllosilicate partial melting in segregating tungsten and tin deposits in W-Sn metallogenetic provinces. *Geology* 50, 121–125.
- Zhou, Z.H., Mao, J.W., Lyckberg, P., 2012. Geochronology and isotopic geochemistry of the A-type granites from the Huanggang Sn-Fe deposit, southern Great Hinggan Range, NE China: implication for their origin and tectonic setting. *J. Asian Earth Sci.* 49, 272–286.
- Zhou, Z.H., Mao, J.W., Wu, X.L., Ouyang, H.G., 2015. Geochronology and geochemistry constraints of the Early Cretaceous Taibaidai porphyry Cu deposit, northeast China, and its tectonic significance. *J. Asian Earth Sci.* 103, 212–228.
- Zhou, Z.H., Breiter, K., Wilde, S.A., Gao, X., Burnham, A.D., Ma, X., Zhao, J., 2022b. Ta-Nb mineralization in the shallow-level highly-evolved P-poor Shihuiyao granite, Northeast China. *Lithos* 416, 106655.
- Zhou, Z., Mao, J., 2022. Metallogenetic patterns and ore deposit model of the tin polymetallic deposits in the southern segment of Great Xing'an Range. *Earth Sci. Front.* 29, 176 in Chinese with English abstract.
- Zhou, Z.H., Mao, J.W., Zhao, J.Q., Gao, X., Weyer, S., Horn, I., Holtz, F., Sossi, P., Wang, D.C., 2022a. Tin isotopes as geochemical tracers of ore-forming processes with Sn mineralization. *Am. Mineral.* <https://doi.org/10.2138/am-2022-8200>.
- Zhou, J.B., Wilde, S.A., Zhang, X.Z., Ren, S.M., Zheng, C.Q., 2011. Early Paleozoic metamorphic rocks of the Erguna block in the Great Xing'an Range, NE China: evidence for the timing of magmatic and metamorphic events and their tectonic implications. *Tectonophysics* 499, 105–117.
- Zhou, J.B., Wilde, S.A., 2013. The crustal accretion history and tectonic evolution of the NE China segment of the Central Asian Orogenic Belt. *Gondwana Res.* 23, 1365–1377.
- Zhu, H., Zhang, L., Du, L., Sui, Q., 2020. The geochemical behavior of tungsten and the genesis of tungsten deposits in South China. *Acta Petrol. Sin.* 36, 13–22 in Chinese with English abstract.